Driving Forbidden Vibrational Transitions in Molecular Oxygen

Annika Lunstad

Advisor: Professor David Hanneke
May 19, 2021

Submitted to the
Department of Physics & Astronomy of Amherst College
in partial fulfilment of the
requirements for the degree of
Bachelors of Arts with honors

Abstract

Recent developments within the field of atomic, molecular, and optical physics have allowed for breakthroughs in the ability to control and interrogate quantized systems. These advances have had large implications in many lines of research, such as high-precision spectroscopy used for clocks and tests of fundamental physics.

We are working towards precision spectroscopy of vibrational levels in molecular oxygen. Our ultimate goal is to measure the transition between two vibrational levels in the ground electronic state of O_2^+. This narrow transition is sensitive to changes in the ratio of the proton mass to the electron mass (μ), which is a fundamental constant found in multiple areas of physics. Several theories of new physics (physics "Beyond the Standard Model") predict that this fundamental constant might drift or oscillate in time.

This thesis presents our first attempts to drive the transition between the ground and 16^{th} vibrational state in O_2^+ $|X^2\Pi_g\rangle$. We carry out our experiment in a beam of oxygen molecules using a two-photon transition. This thesis begins with a discussion of how experiments like our own can contribute to testing Beyond the Standard Model theories which predict that μ will slightly change in time, including models of ultralight dark matter. Next, I describe the current state of our experimental apparatus, with particular attention to recent improvements designed to increase the reliability of our system. Then, I discuss the most recent results of our work: optimizing the timing of our gas and laser pulses to get a cold beam, characterizing this beam, choosing an ionization wavenumber to determine our initial states, identifying the region of interest for our frequency scans, and running scans looking for the vibrational spectrum. Since we have not seen clear indications of resonant, two-photon transitions yet, I discuss challenges and surprises we have encountered. Finally, the thesis concludes with a look to the future for what changes may help us to measure this vibrational spectrum and the long-term outlook of this experiment.

Acknowledgments

First of all, I will be wholly unable to thank Professor Hanneke enough for his teaching and mentorship both during my thesis and throughout my time at Amherst College. His kindness and patience in teaching has instilled confidence in me to ask all of the many, many questions I had and simply enjoy learning. I am so thankful for all of the time and support he has given me during this thesis, both in the detailed feedback and long discussions about my points of confusion. Overall, I am grateful to have been able to work in his lab these last three years, where going to lab was often one of my favorite parts of the week.

I am greatly indebted to my professors throughout my time at Amherst, particularly in the Physics and Astronomy and Math departments, who have taught me so much and supported me along the way. I am thankful also to Jim Kubasek for all of his help throughout my time in the lab.

I additionally want to thank the other students in the lab, especially Boran Kuzhan, Addison Hartman, and Julia Pfatteicher whose work I relied on for this thesis and whose presence made lab even more fun! I am additionally grateful for all of the support of my fellow majors, especially Maria with whom I spent countless hours both writing our theses and working on graduate applications.

I also want to thank my dear friends ('Stranger Gals'!) who have been such a base of love and support throughout Amherst. These years would have been impossible without them. I want to especially thank my dear friend and roommate Sabrina, whose friendship, thoughtfulness, and 'judgemental presence' has truly meant the

world to me.

To my family, thank you for all of your love and support. Especially during this past year with seven people all in the same house for many months, I am thankful that I was able to go through it with all of you. At this academic milestone, I want to particularly thank my mom who was my first teacher and so dedicated herself to the education of both me and my siblings. To my dad, thank you for always being willing to talk about physics with me, from reading my lab reports freshman year to being one of the first to read my thesis. To my siblings, I love you and I believe in you!

Thank you also to Andrew, who has so kindly supported me throughout this thesis and even through a pandemic! I have greatly appreciated your kindness, perspective, and your reminders to take breaks. I cannot imagine going through these last few years without you.

This document is based upon work supported by the Amherst College Provost and Dean of the Faculty and by the National Science Foundation under grant PHY-1806223 (RUI).

Contents

List of Figures

Chapter 1

Introduction

We have an ultimate goal to aid in the creation of new, better clocks based on molecules and using such molecules to test theories of new physics.

Part of the beauty of a tabletop physics experiment is its ability to tie together problems in understanding fundamental physics and problems with electronics, code, temperature control, and even sometimes plumbing. No one thesis can do perfect justice to any of these topics, in fairness. Yet, I hope throughout this document to both motivate why our work matters in terms of the big science goals, as well as why my immediate work, fixing issues with lasers, timing, etc., poses interesting challenges itself.

The objective of my thesis was to attempt to drive forbidden vibrational transitions in molecular oxygen. These transitions are interesting because they are narrow *and* sensitive to changes in a fundamental constant $\mu = m_p/m_e$, where m_p is the mass of a proton and m_e is the mass of an electron.

These transitions are narrow and are so nearly immune to outside perturbations from the environment that they can provide a frequency reference. This ability would allow our molecule to someday serve as a clock and/or a test for new physics.

However, while experimentally testing new physics theories is exciting and impor-

tant, it will take likely several more theses to achieve. My contribution along the way was to bring us closer to measuring a more precise spectrum for transitions from the ground vibrational state in ionized molecular oxygen to the 16^{th} vibrational state. While we have not seen any definitive signal of these resonances, I will show that our work has improved our understanding of the current system, what problems remain, and where some questions still lie.

1.1 Our 'cast and characters'

Before discussing my work in particular, I want to give an overview of some important aspects of our experiment. We eventually want to do high-precision spectroscopy of a vibrational transition in molecular oxygen. These vibrational lines are narrow and, in our planned system, should be immune to several systematic effects. Here, I will give a brief discussion of our system, and a couple reasons why it was chosen.

Our molecule of choice is oxygen, particularly $^{16}O_2^+$. The isotope ^{16}O is the most naturally abundant, making up about 99.76% of oxygen [5]. Furthermore, this molecule has no nuclear spin, and since it is a homonuclear molecule, it is nonpolar. This nuclear symmetry leads to electronic symmetry, which results in all of the rotational states with the 'wrong' symmetry being missing [5, 16]. Thus, half of the rotational states are eliminated and all of the remaining states have the same parity [5].

This question of symmetry is particularly important for us, because we wish to drive vibrational transitions within the same electronic state. Because these two states in the transition will have the same parity (i.e. same symmetry), the transition is electric-dipole forbidden, hence the title of my thesis: "driving *forbidden* vibrational transitions." Since these transitions are electric-dipole forbidden, we must use some other method to drive them. The two, general options are to use the electric-

quadropole moment to drive the transition or to drive a two-photon transition through another electronic state. In our case, we drive the two-photon transitions through an excited electronic state, $A^2\Pi_u$. These two-photon transitions may be thought of as using one photon to off-resonantly drive a $|X^2\Pi_g, v = 0\rangle \rightarrow |A^2\Pi_u\rangle$ transition and then the other photon drives the transition down $|A^2\Pi_u\rangle \rightarrow |X^2\Pi_g, v = 16\rangle$.[1] Thus, we end up with a total transition from the $v = 0$ (ground vibrational) state to the $v = 16$ (excited vibrational) state, both in the electronic state of $X^2\Pi_g$ [5].

Driving two-photon transitions means that we can have transitions with higher Δv (v is the vibrational quantum number), which gives us enhanced sensitivity to μ [5]. Another group plans on using the same molecule but driving an electric-quadropole transition, which means that different excited vibrational states are used [51].

In order to drive these forbidden transitions in O_2^+, we must first ionize neutral O_2. We use a laser to ionize neutral oxygen, a process called photoionization. This method allows us to ionize into a particular rotational state. Next, we drive the transition of interest from $v = 0$ to the $v = 16$ vibrational level in O_2^+ $|X^2\Pi_g\rangle$.

Once some portion of the molecules have made this transition, we need to discriminate between the vibrationally excited molecules and those still in the ground state. In order to do this, we use a laser pulse to dissociate any of the excited molecules, a process known as photodissociation. The resulting amount of oxygen atomic and molecular ions is found by using an electric field to accelerate all ionized particles toward a detector. Because the velocity depends on mass, the molecules and atoms will arrive at the detector at different times, allowing us to distinguish between them. This apparatus is called a time-of-flight mass spectrometer. I discuss the apparatus of this experiment more in Chapter 3.

Currently, we are still a ways from achieving the eventual levels of precision. The

[1] For those new to this notation, I would recommend the Wikipedia page 'Molecular Term Symbol'. For this thesis, it is only necessary to know that different electronic states are designated with a letter, such as X or A. The following Greek letter (like Σ or Π) and the superscript refer to the angular momentum of the state. The subscript (g or u) designates the parity.

focus of my thesis was to drive these vibrational transitions for the first time, and we hope to eventually get more precision on the location of these lines.

1.2 Our experimental context

To provide some context for our work, I will briefly mention below the current best limits on drifts in μ from AMO physics and give an overview of some other experiments using diatomic molecules to look for such drifts in μ.

The current best limit on drifts in μ from an atomic clock comes from comparing a Yb^+ clock to a microwave transition in Cs, where the μ dependence comes from the cesium nuclear magnetic dipole moment [9, 17]; the limit is

$$\dot{\mu}/\mu = (-0.8 \pm 3.6) \times 10^{-17}\ \mathrm{yr}^{-1}. \tag{1.1}$$

Because molecular experiments have the potential to be more precise measurements of changes in μ than atomic experiments, we are also interested in the current best limit from a molecular experiment. Currently, the best measurement is from comparing two vibrational levels between different electronic potentials in KRb [22] and this experiment gives a limit of

$$\dot{\mu}/\mu = (-0.30 \pm 1.0) \times 10^{-14}\ \mathrm{yr}^{-1}. \tag{1.2}$$

Many experiments with diatomic molecules, including our own, have the potential to reach even more stringent limits. This next discussion will be an abbreviated version of part of our recent review paper, where we go into greater detail on the following experiments [17].

In addition to the experiment with KRb mentioned above [22] and the planned experiment from another group also with O_2^+ [51], there are several more groups

looking into μ variation using diatomic molecules. These molecules include Sr_2 [24, 54], N_2^+ [13, 43], and TeH^+ [23].

Note that simply stating the molecule being used is not nearly sufficient for understanding the experiments. I give this list mainly to give a sense of the context of our experiment. As mentioned previously, a more in-depth discussion is given in [17].

Each of the experiments discussed above are looking for *drifts* in μ over time. In terms of looking for oscillations, we are aware of one group discussing the potential of polyatomic ions, such as SrOH, to be sensitive to oscillations in μ [25].

Now, with some sense of our context, we can move forward to the heart of this thesis.

1.3 Looking forward

Before discussing the details of my work in the lab, I will spend a chapter (Chapter 2) going through just one motivation for our experiment. In particular, I will give a brief overview of why dark matter is believed to exist, and how a molecule might be sensitive to a phenomenon that has only been observed at astronomical scales. I will summarize how this cosmological theory predicts oscillations in μ, which may be measured and/or limited in a table-top physics experiment.

After giving my brief overview of some interesting ideas in fundamental physics, I will discuss the details of the experimental apparatus in Chapter 3, particularly as it pertains to my goal of driving 2-photon vibrational transitions. This description of our apparatus will set us up to consider what results we have seen in Chapter 4.

Because we have not yet seen any vibrational transition spectrum, Chapter 4 will also focus on our major roadblocks and what effect they might have had on our work as well as some unexplained surprises. Thus, during the closing Chapter 5, I will build off of our understanding of the current challenges to look to the future, both

short-term and long-term, to suggest some next steps to take and to explain what the lab work might entail in several years.

For now, I will begin with a description of one motivation of our work in the following chapter.

Chapter 2

Motivation

Physics as a field works to create models that describe the material world around us as accurately and simply as possible. In this endeavor, physics continues to face a number of phenomena that require explanations beyond the particles and forces described by the Standard Model of Particle Physics. In particular, the universe seems to contain substantial amount of non-luminous material that greatly increases the masses of galaxies. We call this non-luminous material 'dark matter'.

As theorists work to develop models to explain things like dark matter, the experimental work to either verify or dispute these theories can span several subfields.

Much experimental work in fundamental physics is done by particle physicists in large colliders that create a high-energy environment to search for new physics. Astronomers are able to observe such high-energy physics in the natural world, but they deal with certain constraints. Atomic, molecular, and optical (AMO) physicists can work in a low-energy environment but see the effects of high-energy physics show up as small corrections that would otherwise be forbidden in this low-energy regime [16, 7]. These three areas of experimental work all complement each other in important ways to support experimental research in fundamental physics [7].

AMO assists in these efforts by doing highly precise measurements of energy levels

in atoms or molecules that are sensitive to changes predicted by these new fundamental physics theories

Here, I will give some motivation for the question of dark matter and try to connect this problem to the work we do in our lab.

2.1 Problems in Fundamental Physics

Particle physicists have been working to fit the basic forces and particles we have seen in the universe into one theoretical model. The current model accepted in physics is called the Standard Model. It describes the basic particles that have been detected and three of the four forces that make up everything around us [32].

The model has been a powerful one that explains many phenomena [32]. However, the universe annoyingly remains more complex than our understanding of it. For example, while gravity certainly exists as one of the four forces, it is not yet accommodated by the Standard Model as there is no quantum field theory that can describe it [11]. Additionally, there are reasons to believe that there may be particles and or forces that have not yet been detected or fully explained, such as dark matter.

2.1.1 Brief overview of some deficiencies of the Standard Model

The Standard Model effectively describes most of the phenomena around us, but scientists have found indications of dark matter which do not fit within the Standard Model. Before postulates of dark matter, most scientists supported the theory that the matter that exerts a gravitational force is luminous, and so might be detected through some signal in the electromagnetic spectrum [12, 1]. However, over the last century, scientists have come to the realization that, in fact, there is a kind of 'dark' (non-luminous) matter that cannot be directly detected via any known methods and

is actually more abundant than our known, ordinary matter [12, 1]. We have seen the effects of this dark matter, as it exerts a gravitational force on astronomical objects, but we have not yet directly detected dark matter and much remains to be learned about it.

This evidence for dark matter came primarily from astronomers. For example, work done by Vera Rubin studying the rotation of galaxies found that the velocities of stars, particularly those on the edge of galaxies, could not be explained using the known laws of gravity and the luminous mass seen in the galaxies [12]. Essentially, the stars on the edges of galaxies seemed to rotate as quickly as stars in the center, which contradicts models of rotation velocities based on the luminous mass, which is concentrated at the center of galaxies [12]. Whereas stars and planets (made of luminous mass) are concentrated at the center of galaxies, dark matter seems to form a halo around the galaxies [12].

Another way of seeing the effects of dark matter in the universe is gravitational lensing. This technique relies on Einstein's General Theory of Relativity, which says that spacetime is distorted by massive objects. Thus, anything (including light) that travels through this spacetime will follow a path that is slightly distorted by any massive objects along the path. Astronomers found that the light from some bright object like a galaxy could be distorted into an 'arclet' if there was another massive object nearly in front of it [12]. The amount that a source is distorted (the radius of the arclet) can be used to infer the mass of the object that caused the distortion [12]. Scientists found that the mass calculated using gravitational lensing was much larger than the luminous mass [12].

These are just a few examples of experimental evidence of many from astronomy that point to the need for some explanation of what this dark matter is.

2.1.2 How can we translate an astrophysics problem to table-top physics?

The large amount of evidence, which was only hinted at above, greatly motivates the need for a theory of dark matter and gives some clarity of what to look for. Theorists have suggested many possible explanations and potential particles, often called dark-matter candidates, to explain what we have seen. However, the task to both suggest and then find evidence for or against a dark-matter candidate is enormous.

This thesis cannot even begin to give a real overview of the different theories. For readers interested in learning more, I would recommend [1, 12, 30] based on my own readings. For a more comprehensive discussion of the Standard Model, see [32].

Some of these theories predict slight changes or shifts in fundamental constants. These fundamental constants are unitless constants that are important to physics, with some examples being the fine-structure constant α or the proton-to-electron mass ratio μ. These effects can be measured in a table-top physics experiment. I will focus on one theory for temporal changes in μ as a result of dark matter below

Oscillations in the proton-to-electron mass ratio

One historically popular theory for dark matter is WIMPs (Weakly Interacting Massive Particles), which are non-luminous and so far undetected but could explain dark matter [12, 30]. These dark-matter candidates act like particles in that they could (weakly) interact with other particles and hit a detector, and several detection experiments are underway [30]. So far no WIMPs have been detected.

Because no WIMPs have been detected so far, it is important to consider other, theoretically motivated, non-wimpy ideas for dark matter. One theory I wish to discuss here is a bosonic scalar field of ultralight dark matter, as described in [18, 46].

These scalar fields would be created by dark matter that is so light that the particle wavepackets overlap and create a classical field [46]. If new couplings between these

theorized particles and Standard Model particles existed, the oscillations in the field would translate to oscillations in fundamental constants, like $\mu = m_p/m_e$ [17]. There are several models for the coupling of this dark-matter field to μ, and this fundamental constant is sensitive to couplings to gluons, quarks, the Higgs, or electrons [17].

Within these models for ultralight dark matter, there is still a range of possible masses. For example, these masses could span the range of $m \sim 10^{-21}$ eV/c^2 (the wavepacket would be roughly the size of a small dwarf galaxy) to $m \sim 10^{-1}$ eV/c^2 (the upper bound for the wavepackets still creating a classical field) [46, 47]. Given that the field would oscillate by the Compton frequency, $f_\phi = m_\phi c^2/h$, this range of masses can be translated into a range in frequencies: $10^{-7} - 10^{13}$ Hz [17].

This oscillating, classical field (labeled as ϕ) has an oscillation frequency given by the mass, as discussed above. To find the amplitude of the oscillating field (ϕ_0), we must consider the field's energy density (ρ_ϕ) [17]. If we suppose that this field makes up the majority of the galaxy's dark matter, we can estimate the energy density as $\rho_{\rm DM} \approx 0.4$ GeV cm^{-3} [6]. We can use this value in our equation for the field amplitude [17]:

$$\phi_0 = \sqrt{\frac{\hbar^3}{c^5}}\frac{\sqrt{2\rho_\phi}}{m_\phi}. \tag{2.1}$$

If we suppose that the energy density of dark matter is entirely comprised of this field, then $\rho_\phi = \phi_{\rm DM}$. This equation gives the oscillation amplitude for the dark matter for different masses of the dark-matter particles. Then, this field can couple to the proton and/or electron. Subection 2.2.1 will discuss constraints on the coupling constants, which connect oscillations in the dark-matter field to oscillations in μ.

Thus, an experiment looking for oscillations of μ can focus on the given range in frequencies and then use the oscillation amplitude to calculate the sensitivities of our experiment to oscillations for this range. In order to continue the discussion of sensitivities to fundamental constants, I need to step back and describe the project

of precision measurements in molecules.

Precision Measurements

High precision spectroscopy is important to modern physics, leading to new clocks that redefine the second as well as tests of fundamental physics, like the electron electric dipole moment. Precision measurements (as a class of experiments) often revolve around better measurements of a fundamental constant or a change in a fundamental constant without necessarily measuring the constant itself; ours is the latter [35]. When looking for slight change in a fundamental constant, a precision measurement experiment requires a system that is both sensitive to the fundamental constant in question *and* is not able to be easily perturbed by the environment.

High precision spectroscopy with atoms is well-developed, but the possibilities for increased sensitivity in molecules has lead to greater interest in improving molecular spectroscopy.

2.2 Searches for Time-Variation of Fundamental Constants with Molecules

Developments in laser technology and other breakthroughs have allowed for new advances in precision measurements, particularly with atoms. For example, a recent result from JILA showed that strontium atoms in an optical lattice could get to a relative (fractional) frequency stability of $5.2(3) \times 10^{-17}\ \tau^{-1/2}$, where τ is the averaging time, expressed in seconds [53]. These results, and many other results that have even lead to redefining the second, are based in substantial work to precisely control atoms.

Guided by the work with atomic systems, molecules have been receiving increased interest due to both the exciting opportunities and challenges that they present.

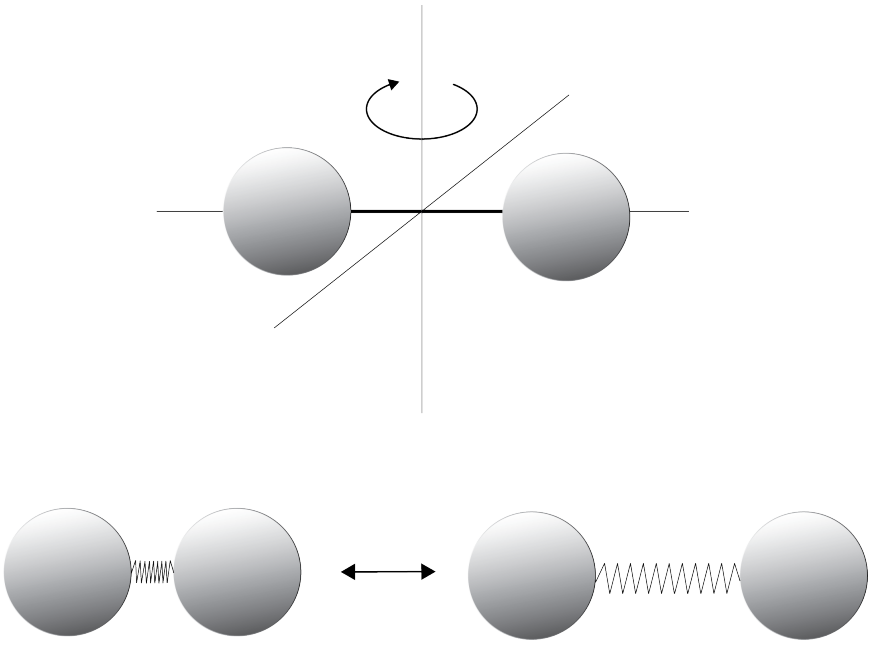

Figure 2.1: This figure shows degrees of freedom, namely rotation and vibration, that are available in molecules but not atoms. This drawing is highly simplistic as it represents the masses on a spring model of a molecule, but it offers a good intuition of the relevant differences. Furthermore, this figure focuses on the rotation and vibration of diatomic molecules specifically.

2.2.1 Precision Measurements with Molecules

Molecules can be more challenging, and in some cases more rewarding, because of the many energy levels and degrees of freedom available. Essentially, because there are multiple atoms in a molecule, they are able to vibrate or rotate relative to the others, as seen in Figure 2.1. These new degrees of freedom lead to other energy levels (called rovibrational states) within molecules.

These rotational and vibrational states can make typical techniques used in atom cooling and control, such as optical pumping, more difficult. However, these additional states can lead to increased sensitivities to new physics or possibilities for new experiments via interactions possible in molecules.

In order to have a precision measurement experiment, you first need a system that is sensitive to the fundamental constant of interest. In the Hanneke lab we

study oxygen molecules, $^{16}O_2^+$ specifically, to search for changes in $\mu = m_p/m_e$. The vibrational levels in this molecule are sensitive to changes in the mass ratio, through a simple model [5].

We must now discuss the sensitivity of O_2^+ to oscillations in μ and the precision that we expect to be able to reach, in comparison to the current leading measurements.

Sensitivity to μ Oscillations in O_2^+

The vibrational levels in diatomic molecules are sensitive to changes in μ through the relatively simple model of two masses on a spring. We must then understand how to connect the sensitivity of these energy levels to changes in μ.

To look for changes in μ, we want to measure the energy difference between two states that depend differently on μ [5]. Thus, we monitor the frequency from

$$hf = E'(\mu) - E''(\mu) \tag{2.2}$$

and we can relate any shift that we see in the frequency (and thus in the energies) to a shift in μ [5]:

$$\frac{\Delta\mu}{\mu} = \frac{\Delta f}{f_\mu}. \tag{2.3}$$

The value f_μ is called the absolute sensitivity and is given by

$$f_\mu \equiv \mu\frac{\delta f}{\delta\mu} = \frac{\delta f}{\delta(\ln\mu)}; \tag{2.4}$$

this value is also called the 'absolute enhancement factor.'

Thus, we have connected the energy difference between two states to the frequency (Equation 2.2) and then the shift in measured frequencies to a shift in μ (Equation 2.3). Next, we must decide which two energy levels will allow for the greatest sensitivity, while remaining nearly immune to environmental perturbations.

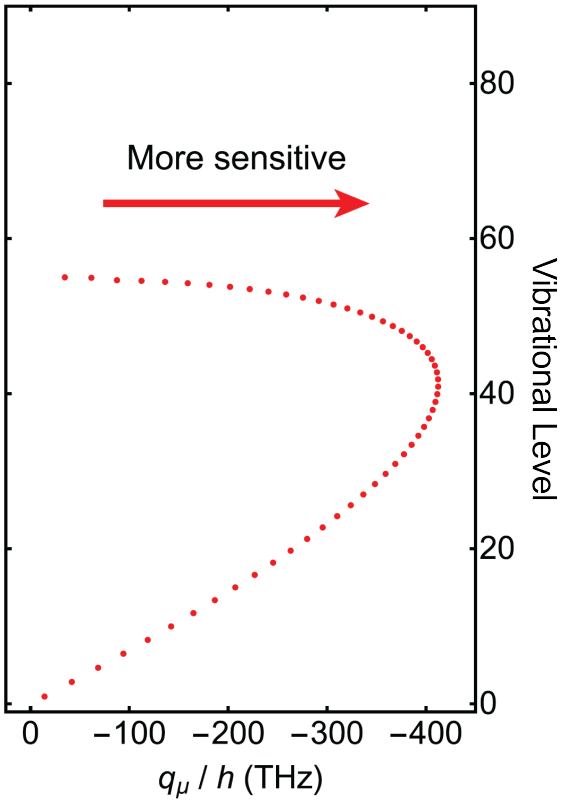

Figure 2.2: This plot gives the sensitivities of the various vibrational levels in O_2^+ in the ground $^2\Pi_g$ state. The absolute sensitivity (q_μ) is given by $hc[-\omega_e(v+1/2)/2 + \omega_e x_e(v+1/2)^2 - B_e J(J+1)]$, where I use terms defined in [17]. We currently plan to excite transitions to the 16^{th} vibrational level. This plot is adapted from [17] and used within the terms of the reference's CC license.

It seems natural that changes in the mass ratio $\mu = m_p/m_e$ would cause changes to the energy of a diatomic molecule in this model as m_p contributes to the masses at the end of the spring (the atoms) and m_e contributes to the spring constant (chemical bond) for the vibrating molecule.

To slightly rephrase, the most basic approximation of a vibrating molecule is as a harmonic oscillator and, thus, we can give the potential energy for a homonuclear diatomic molecule as:

$$V = \frac{1}{2}k(r - r_e)^2, \tag{2.5}$$

where r_e is the equilibrium distance between the two atoms and k is the spring force

constant [4].

Converting this classical description and potential into a quantum mechanics problem, one can solve the Schrödinger Equation and get energy levels:

$$E_v = h f_{osc} \left(v + \frac{1}{2} \right),$$

where h is Planck's constant, v is the vibrational quantum number, and f_{osc} is the harmonic vibrational frequency in Hz [4]. In our work, we tend to talk about the harmonic vibrational frequency in units of wavenumbers (cm^{-1}) and written as $\omega_e = f_{osc}/c$. Additionally, and most importantly for us, we can get the frequency of oscillation in wavenumbers as,

$$\omega_e = \frac{f_{osc}}{c} = \frac{1}{2\pi^2 c}\sqrt{\frac{k}{m}}, \tag{2.6}$$

where m is the reduced mass of a homonuclear, diatomic molecule (and not the standard μ to avoid confusion with two meanings of μ) [4]. Here, m is the mass of the nucleus which is directly related to m_p (the mass of a proton), and k is the spring constant which is related to the mass of the electron, m_e. Using dimensional analysis, we can see that the mass of the nucleus, m, in the denominator (which depends linearly on m_p) needs to cancel with a mass in the numerator (m_e, the only other mass in this system) in order to get the correct constants. Since m_e contributes to the spring constant k, we can say that the vibrational coefficient ω_e scales with $1/\sqrt{\mu}$ [16].

Thus, the vibrational coefficient scales with $1/\sqrt{\mu}$, and our vibrational sensitivity increases linearly with the vibrational quantum number v [5].[1] The rotational states also have a high sensitivity (which scales as $1/\mu$). However, the selection rules for rotational states mean that we could only drive transitions with small ΔJ (J being

[1]The terms in the sensitivity are $-\omega_e(v+1/2)/2+\omega_e x_e(v+1/2)^2$ [17]. So, for smaller v, the first term dominates and the sensitivity increases linearly with v. At higher v, the second term begins to cut into the sensitivity [17]. These characteristics of the sensitivity can be seen in Figure 2.2.

the rotational quantum number) [5]. The transitions between vibrational levels are dictated by Frank-Condon factors, and not selection rules as such, and so it is possible to drive transitions with larger Δv. Additionally, looking back to Figure 2.2, we can see the sensitivity increasing with v, up to a point. Thus, being able to drive a transition with $\Delta v > 1$ is particularly useful.

Ultimately, this simple model is important because any measured oscillations (or lack thereof) in f could be connected to oscillations in μ with a high degree of confidence since the theory to connect them is simple and well-understood. This leads some physicists to call the measurements "model-independent," as opposed to a highly 'model-dependent' measurement that would only be relevant for a more contested or complicated model.

Projected precision needed for our experiment

Given that we have established that the vibrational levels in our molecule are sensitive to oscillations in μ, we must consider whether we can get the requisite level of precision. These calculations and a discussed of the systematics for our experiment are discussion in [5]. Our projected level of precision must also be compared to the current best measurements of oscillations in μ, which I will discuss in greater detail here.

There are several experiments looking for *drifts* in μ, ours among them. When looking for drifts in μ, there are sets of constraints from various experiments (astronomical, atomic, and molecular) to consider, as I discussed in Chapter 1.

To focus on potential oscillations in μ, there have not yet been any experiments to directly constrain oscillations in μ, to our knowledge. Thus, these limits are estimated based on models for the dark-matter coupling and constraints on the coupling coefficients given by tests of the Equivalence Principle [17].

The following discussion is an abbreviated version of part of our recent paper [17].

In order to understand what we are constraining, consider a model where the dark-matter field only couples to the gluons to give the oscillation amplitude in $\Delta\mu/\mu$ as given by the below:

$$\frac{\Delta\mu}{\mu} = d_g\phi_0\sqrt{\frac{4\pi G}{\hbar c}} = \frac{d_g\sqrt{\rho_\phi}}{m_\phi}\frac{\hbar\sqrt{8\pi G}}{c^3}, \tag{2.7}$$

where G is the Newtonian gravitational constant and we use the field amplitude from Equation 2.1 [2, 18]. Additionally, we assume that $\rho_\phi = \rho_{\rm DM} \approx 0.4$ GeV cm^{-3}, which is the estimated energy density of dark matter in the galaxy, as discussed in Subsection 2.1.2 [6].

Within the range of masses (10^{-21} eV/c^2 – 10^{-1} eV/c^2), we have two different constraints on the dark matter coupling constant d_g from equivalence principle tests. For $m_\phi < 3\times10^{-14}$ eV/c^2, torsion balance experiments have restricted the coupling coefficient to $|d_g| < 7.2\times10^{-6}$ [38]. For higher masses in the range 3×10^{-14} eV/c^2 – 10^{-1} eV/c^2, other restrictions give us $|d_g| < 3\times10^{-2}$ [18, 2]. Thus, using these constraints and Equation 2.7, we get oscillation amplitude in μ of [17]

$$\frac{|\Delta\mu|}{\mu} < \begin{cases} 5\times10^{-36}\ \text{eV}/(m_\phi c^2), & m_\phi < 3\times10^{-14}\ \text{eV}/c^2 \\ 2\times10^{-32}\ \text{eV}/(m_\phi c^2), & m_\phi > 3\times10^{-14}\ \text{eV}/c^2 \end{cases}. \tag{2.8}$$

Again, using the Compton frequency, these limits may be translated into limits that depend on the frequency of oscillations, as shown here [17]

$$\frac{|\Delta\mu|}{\mu} < \begin{cases} 1\times10^{-21}\ \text{Hz}/f_\phi, & f_\phi < 7\ \text{Hz} \\ 5\times10^{-18}\ \text{Hz}/f_\phi, & f_\phi > 7\ \text{Hz} \end{cases}. \tag{2.9}$$

Given Equation 2.9, it is important to keep in mind that the limits on μ oscillations depend on the frequency of oscillation we are looking for and compare those limits to

our projected precision. Ultimately, we should be able to reach a precision of 10^{-18} in our measurement of $\delta f/f_\mu$ [5]. Our experiment, and other molecular experiments like it, would have the most to contribute at the low-mass end of the range, because Equation 2.8 predicts that the constraints on low-mass are loose enough that our system can improve upon them.

A look forward

This chapter gave a particularly broad look at our experiment and how it fits into physics as a whole, as well as some of the details of one model. However, there are still many steps we need to take to bring the experiment to the point of reaching these high levels of precision. In the rest of the thesis, I will describe our efforts to drive a two-photon vibrational transition in molecular oxygen. We have not actually seen a vibrational transition spectrum yet and, even if we did, it would not yet be at the projected 10^{-18} precision. Regardless, our work still takes important steps in the direction of our larger goal.

I will describe our experimental apparatus in greater detail. I will also cover what we saw and, particularly, what remains unexplained in our experiment.

Chapter 3

Experimental Apparatus

In order to reach our science goal of precisely measuring these vibrational transitions, we must first solve many interesting challenges in building the apparatus.

Currently, we are working with oxygen molecules in a beam. We first photoionize a large number of molecules into a few rotational states. Secondly, we excite the vibrational transition and, finally, dissociate any molecules that have been vibrationally excited.

In this chapter, I will walk through our experiment in more detail and describe the apparatus that helps us reach our scientific goals.

3.1 Overview of the experiment

We aim to see the frequency spectrum for transitions from $^{16}O_2^+$ $|X^2\Pi_{g,\frac{1}{2}}, v = 0\rangle$ to a vibrationally excited state in the same electronic potential, such as the 16^{th} vibrational state. Ultimately, we are interested in transitions from our science state $^{16}O_2^+$ $|X^2\Pi_{g,\frac{1}{2}}, v = 0, J = 1/2\rangle$ to an excited vibrational state, since the $J = 1/2$ has more favorable systematics [5]. For my thesis, our primary goal is to simply see the resonant transitions from any rotational state in the ground vibrational state to an excited vibrational state.

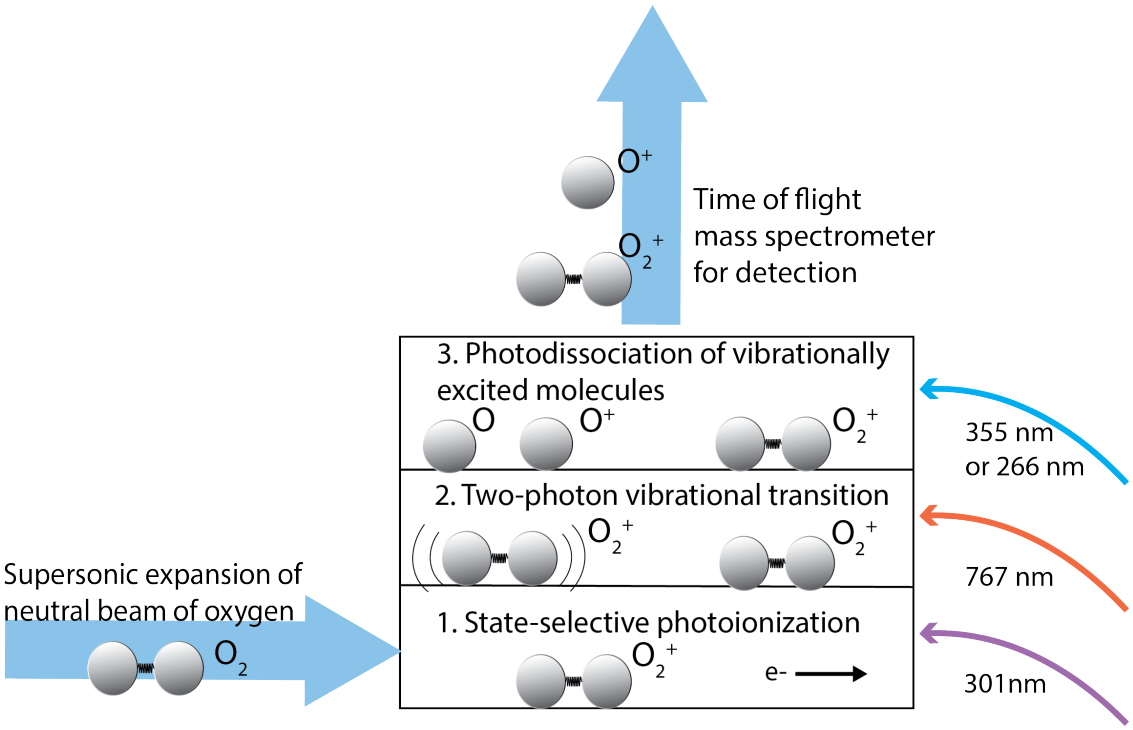

Figure 3.1: A block diagram overview of the experiment. The molecules start on the left. The steps in the central box all occur in the same location in space, before being accelerated up to the detector. The arrows on the right represent the general wavelengths of the laser we use for each transition, and they are also spatially overlapped in the actual experiment.

We start with a beam of neutral molecules (on the left in Figure 3.1). The beam expands supersonically and cools, which populates the lower rotational states [10]. In order to get molecules in the correct initial state of the ionized molecule, we photoionize them using a 2+1 Resonance Enhanced Multi-Photon Ionization (REMPI) scheme [5, 10]. This is step 1 in Figure 3.1. After exciting the two-photon vibrational transition (Step 2), we use photodissociation to selectively dissociate any molecules that made the transition (Step 3). In order to differentiate between the molecules and atoms, we use a time-of-flight mass spectrometer.

The sequence of events must be precisely timed. We use a hardware timing device (PXI-6534) to send out triggers in the correct sequence. This sequence is, in turn, determined by a LabView program where we can adjust several aspects of the timing

as necessary. While the computer's clock has low jitter, it has a clock cycle of 20 MHz, and, especially for the lasers (Steps 1-3 in Figure 3.1), we want there to be about 15 ns between each beam arriving in the experimental region so that we do not lose signal due to molecules flying out of the experimental region before all steps of the experiment can occur. This more precise timing is achieved using coaxial cable length and optical path length. The details are discussed further in Appendix B.

Now, with the overall goals in mind, we can discuss the various steps of the experiment in greater detail.

3.2 Molecular Beam

In order to have decent statistics, we need to be able to do our experiment with as many molecules as possible for each run. Here, I will outline our requirements for the molecular beam, and how we achieve them.

Neutral molecules in the ground electronic state ($X^2\Sigma_g$) are excited to a Rydberg state ($d^1\Pi_g$) in the neutral molecule [5]. Any of the first four rotational states in the Rydberg state, $^{16}O_2$ $|d^1\Pi_g, v' = 0, N = 1, 2, 3, 4\rangle$, can reach the ground rovibrational state in the ion, which is $^{16}O_2^+$ $|X^2\Pi_{g,\frac{1}{2}}, v = 0, J = 1/2\rangle$ [5]. The molecular potentials, as well as our transitions, are shown in Figure 3.2. Because only the first four rotational states in the neutral Rydberg state can be ionized into the correct state in the molecular ion, we want as many molecules as possible in these first four rotational states. We can select one of these states spectroscopically. However, the number of molecules in we can excite into these first four rotational states in $d^1\Pi_g$ depends on the temperature of the beam [10]. Specifically, a cool beam will allow a higher number of molecules to be excited into the first four rotational states in the neutral Rydberg state ($d^1\Pi_g$).

Additionally, this experiment needs to be able to run for hours on end, and so

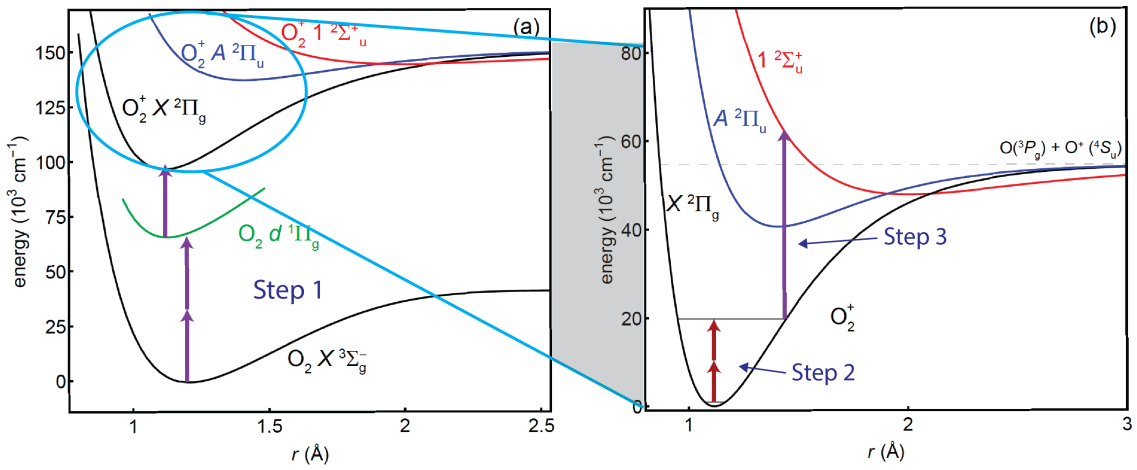

Figure 3.2: These plots show the relevant molecular potentials and the transitions in our experiment. Following Figure 3.1, Step 1 is the REMPI transition, Step 2 is our two-photon vibrational transition, and Step 3 is the photodissociation from the excited vibrational state. Note that the potential $A^2\Pi_g$ is included because we drive the two-photon transition through this state [5]. This figure is adapted from [5].

the turbos cannot be overburdened. Allowing gas to build up in the chamber would potentially damage the MCP (micro-channel-plate detector) as well as causing the gas to reach a warmer equilibrium temperature, thus cutting into our statistics.

To solve these problems, we pulse oxygen into the chamber. This allows the turbos to maintain the necessary level of vacuum. Additionally, going from a high-pressure container to a vacuum, the beam undergoes supersonic expansion, which ultimately means that it is substantially cooled [10]. We then select the cold center of the molecular beam using a skimmer, as seen in Figure 3.3 [10]. This skimmer also helps to limit the amount of gas in the part of the chamber with the delicate MCP. Regardless, we are using a pulsed laser beam at this point in the experiment. So, it is unnecessary to have a continuous beam of molecules.

After the skimmer, the (now) cool beam continues to rush towards the experimental region, which is between the electrodes and visible on the left-hand side of Figure 3.3.

Thus, we now have a beam of neutral molecules, with high populations in the low

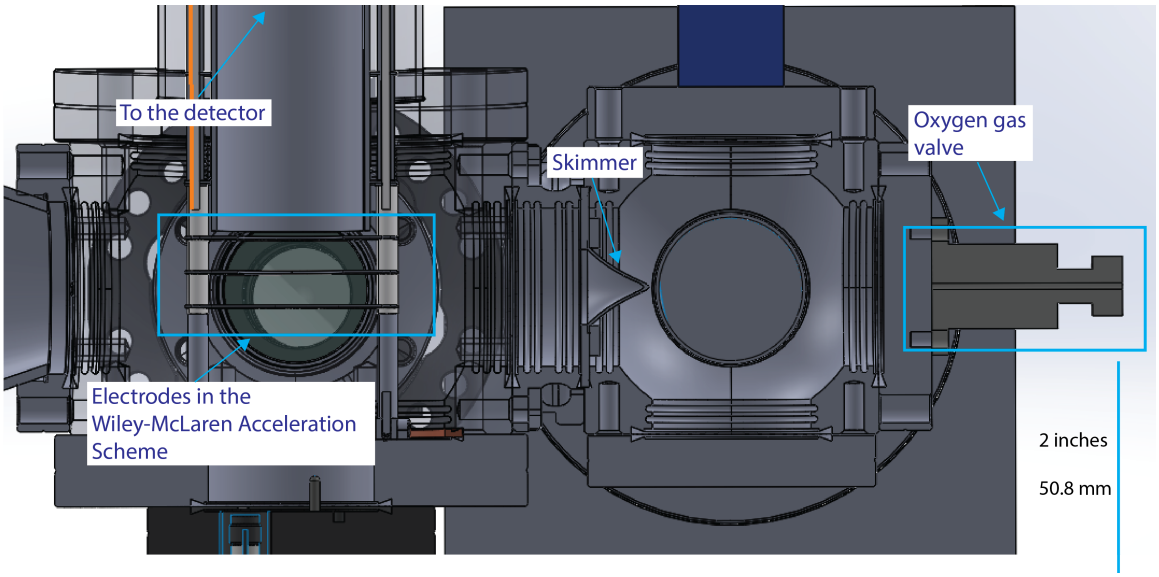

Figure 3.3: A zoomed-in cross-section of the apparatus, focusing on the path of the beam from the valve (on the right), through the skimmer and to the experimental region between the bottom two electrodes. The experiment takes place in between those two lower electrodes, before the molecular and atomic ions are accelerated up to the detector.

rotational states due to the cold temperature. Now, the molecules can be ionized into the correct initial state so that we can begin to probe the vibrational transition.

3.3 Photoionization

The next step in the state preparation for our experiment is photoionization into the state $^{16}O_2^+$ $|X^2\Pi_{g,\frac{1}{2}}, v = 0\rangle$. We use a 2+1 REMPI scheme which photoionizes the molecule by first exciting a two-photon transition to a Rydberg state in the neutral and then exciting the molecule to the ground electronic state of O_2^+ [10]. The last photon has enough energy to excite the molecule to the first vibrational state ($v = 1$), but due to nearly diagonal Franck-Condon factors the majority of molecules end up in the $v = 0$ state [5].

Photoionizing the beam requires high laser intensity; so we use a pulsed laser beam that intercepts the molecular beam in the experimental region (between the first two

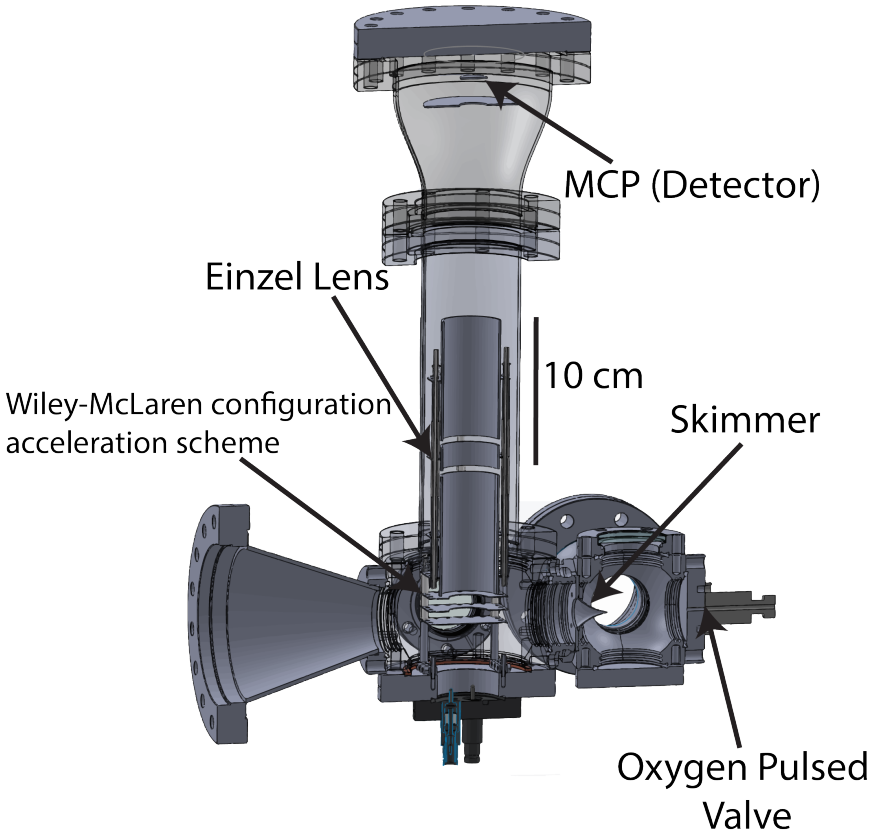

Figure 3.4: A cross section of our apparatus, with labels focusing on the acceleration and detection scheme. The turbos are not pictured.

electrodes in the Wiley-McLaren configuration acceleration scheme in Figure 3.4. The photoionizing beam, which I will call the REMPI beam, originates in a Quantel YQ660 Nd:YAG laser, which lases at 1064 nm and is frequency-doubled to get 532 nm. The 532 nm light then pumps a Quantel dye laser, with a mix of Rhodamine 610 and Rhodamine 640 dissolved in methanol. This dye laser emits light at 602 nm. Next, this 602 nm light is frequency doubled to produce a 301 nm beam, which is what we use for photoionization. The photoionization beam should generally have an energy around 800 μJ, but we have had some issues with the REMPI laser so it was often lower around 200 μJ towards the end of this year.

Note that the gas pulse duration (to control how much gas is released into the chamber) and the gas pulse delay (to control which part of the gas pulse arrives at the

experimental region when the laser does) are additionally important for controlling the temperature of the beam and the amount of ions in the correct initial states. We can control these timings with the electrical trigger to the gas valve (details of triggers are in Appendix B). To open the valve, we send an electrical pulse to a solenoid which pulls back the poppet from the hole. Then, when the electrical pulse stops, a spring pushes the poppet back in place. Pulling back the poppet does not happen instantaneously, which adds to the delay between sending the trigger and the gas arriving to the electrodes. I discuss our optimized parameters in Chapter 4. For now, it is sufficient to know that a significant proportion of our molecules are ionized into the correct initial state.

Currently, we are ionizing at 16591.0 cm^{-1} (which is the dye-laser wavenumber, *not* the wavenumber of the transition itself), which gives us a large portion of molecules in the initial rotational state of N = 2. Our recent work to better understand the beam and photoionization process is discussed in Chapter 4.

The UV photoionization beam (which I will generally refer to as the REMPI beam) then is guided to the experiment chamber and spatially overlapped with the other two beams, which comprise the next two steps in the process. The next stage in the experiment is the vibrational transition.

3.4 Two-photon vibrational transition

Now that we have a large number of molecules in the correct intial state, we drive the two-photon vibrational transition with a beam of 767 nm light. Because this is a two-photon transition, we again need high intensity. At this point, we achieve this both by using a pulsed beam (7 ns) and by ensuring that we have a relatively high energy of around 25 mJ.

Both the vibrational transition beam and dissociation beam originate in our In-

nolas SpitLight Nd:YAG pulsed laser. The fundamental frequency is 1064 nm. It is then frequency doubled to get 532 nm, then the two beams are summed to get our dissociation beam of 355 nm. Using a different crystal, we can get another option by frequency-doubling the 532 nm light to get a beam of 266 nm. The 532 nm beam is used to pump a SIRAH Cobra Stretch dye laser to produce a beam at 767 nm, which we use to excite the two-photon vibrational transition.

The vibrational (767 nm) beam itself is linearly polarized after passing through an optical isolator. Slight angles of the mirrors may lead to it being slightly elliptically polarized, but it can still be approximated as being linearly polarized [16]. This polarization becomes relevant later for our calculations of the two-photon transition probability in Chapter 4.

In our dye laser, we use dye LDS751 dissolved in DMSO (dimethyl sulfoxide). The laser is tuned with a diffraction grating over our region of interest. Our grating has 1800 lines/mm and is 90 mm long, which should allow us to tune from 400 nm to 920 nm. However, our choice in dye will determine our efficiency for wavelengths within this range. We chose our dye based on its high efficiency around 767 nm. We run the laser with output energies at 767 nm between 22-28 mJ. The energy decreases over the course of a day due to the rapidly declining dye efficiency, hence the range instead of a single value. We bring the energy up to around 28 mJ each morning by adding more dye concentrate.

The overall bandwidth of the laser (set by the diffraction grating) is 0.072 cm^{-1} at 767 nm. However, within this profile, the laser has several axial modes, each with a bandwidth of 0.005 cm^{-1} (set by the pump laser duration) and spacing 0.017 cm^{-1} (set by the cavity length). Thus, the laser only has the bandwidth of 0.072 cm^{-1} on average, since each shot will have several axial modes within the overall bandwidth of the laser. This concept is depicted in Figure 3.5.

Since the linewidth of our transition is narrow, we could miss the transition if

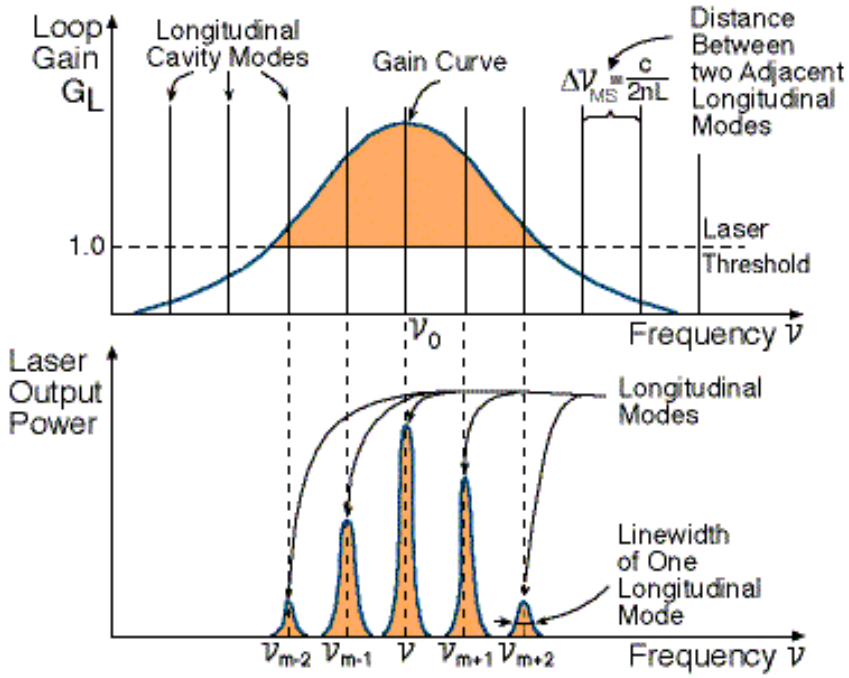

Figure 3.5: This explanation from the University of Toronto shows the gain curve of the laser (given by the diffraction grating for us) and the longitudinal modes (which we also call axial modes). The overlap is shown above and the result given is seen right below. Courtesy of the Laser Safety Manual from the University of Toronto [48].

it happened to fall between two axial modes. Without any intervention, these axial modes might slowly drift with time (perhaps on the timescale of several minutes, see Figure 3.6). This long drift means that we might risk completely missing a resonant transition simply because the axial modes were not at the correct frequency. We address this problem by using a piezo with a triangle wave on it to dither the length of the cavity, which shifts the axial modes. This system is referred to as the Dynamical Mode Option (DMO) by SIRAH, and I will use DMO as shorthand from now on. Since the axial modes are set by the cavity length, dithering the cavity length ensures that the axial modes shift around on a significantly faster timescale. Therefore, the axial modes actually fill up the entirety of the laser bandwidth on average, without needing to wait for minutes at each step. While we do not currently have a wavemeter with high enough resolution to resolve these axial modes, the principle of how the DMO

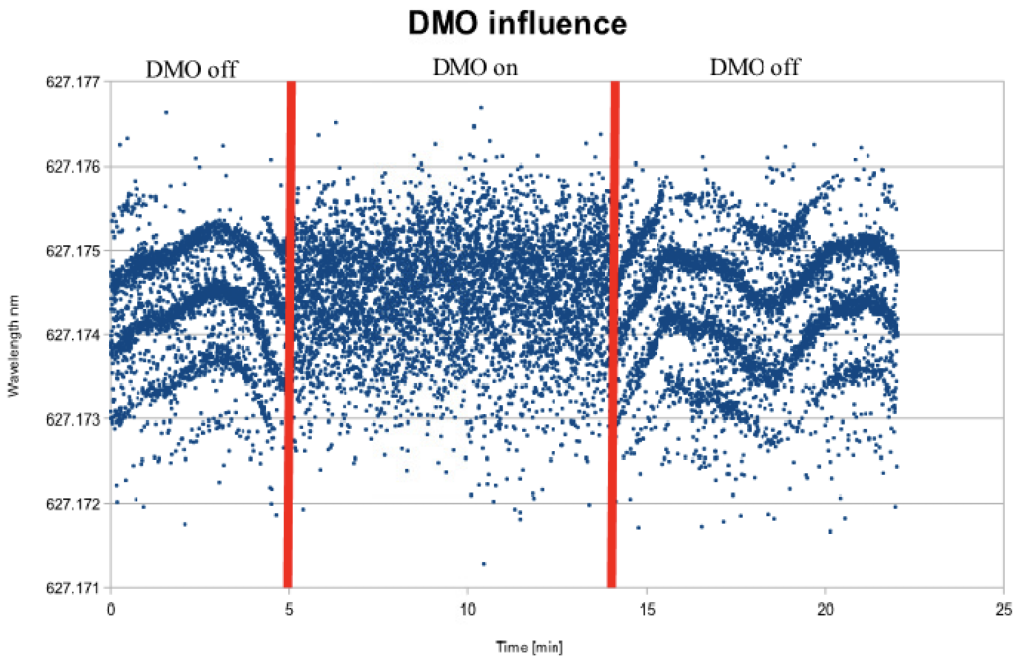

Figure 3.6: This image shows the effect of the DMO on the frequency profile for a SIRAH laser. Note in particular the time scale of several minutes for the slight oscillations. Figure courtesy of Paulus Jauernik from SIRAH laser [21].

should influence the frequency profile of our SIRAH laser is illustrated in Figure 3.6.

Now that we have ensured that the laser will be resonant with the transitions when scanning across them, we must consider how the wavenumber will be calibrated and, eventually, reported. We currently calibrate the laser with a Burleigh Pulsed Wavemeter. In the long-term, we will use a potassium vapor cell in addition to a wavemeter, since potassium has a resonant transition near 767 nm.

The beams are all directed through an achromatic lens to focus in the center of the 'experimental region.' From the perspective in Figure 3.3, the beams come in perpendicularly to the path of the beam from the window directly behind the electrodes (as seen in the figure). In order to cancel the first-order Doppler shift in the vibrational transition, we retroreflect the vibrational beam using a spherical mirror, shown in Figure 3.7. The mirror's placement brings the light to a focus in the same location on the return path. The details of this retroreflection and its alignment

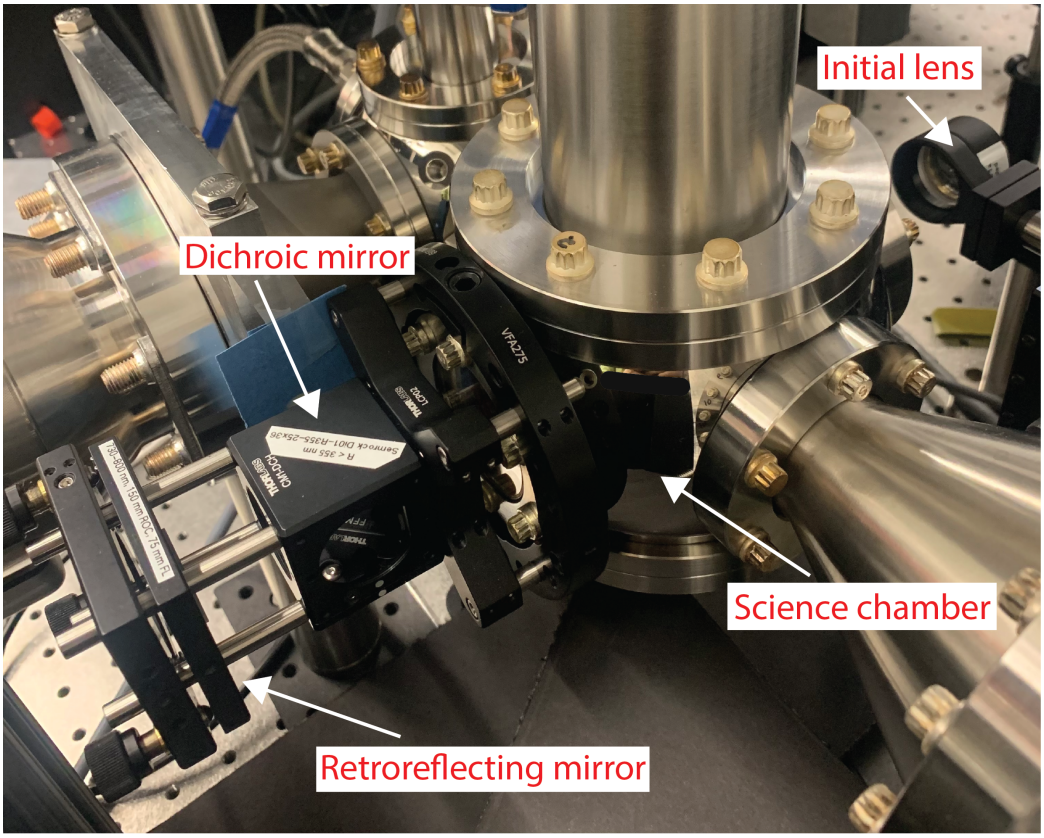

Figure 3.7: A picture of our retroreflection mirror mounted on the cage rods, which connect it to the flange. The initial lens, which focuses our beams, is also pictured, as well as the dichroic mirror, which dumps the UV beams.

are discussed in Appendix A.

3.5 Dissociation

In order to tell whether we made the transition, we need to have some kind of state readout. Eventually, our lab will use quantum logic spectroscopy with O_2^+ and Be^+ in an ion trap. However, because we are currently carrying out the experiment in a molecular beam, we use photodissociation to selectively dissociate any molecules that make the vibrational transition while leaving the molecules in the $v = 0$ state intact. This photodissociation is followed by a time-of-flight mass spectrometer to differentiate the atomic ions from the molecular ions.

Thus, after the 767 nm beam, we follow with a UV beam (with a wavelength of either 355 nm or 266 nm) to dissociate the molecules. As mentioned in Section 3.4, the beam originates in the Innolas Nd:YAG.

The Innolas laser has a convenient design that allows us to switch the crystal for our dissociation beam. By changing the final crystal, we can have a dissociation beam of either 355 nm or 266 nm. Since the cross-section for dissociation is different for the two wavelengths, it is useful to be able to switch between the two wavelengths in roughly an afternoon.

Additionally, by adjusting the angle of this crystal, we can control the energy of the laser pulses. This ability allows for quick adjustments of the dissociation beam energy. We run the 355 nm dissociation beam with an energy of around 15 mJ per pulse most recently (previously, it was around 5 mJ). When we switched to the 266 nm beam, we had to turn down the energy to 3 mJ per pulse because the high-energy photons were photoionizing (see Chapter 4 for details), and we may have to turn the 266-nm beam energy down further.

Since both the vibrational transition beam and the dissociation beam originate in the Innolas laser, their relative timing cannot be controlled electrically. We can control this timing using additional optical path length to get to a relative timing of around 15 ns (refer to Appendix B, particularly Figure B.2, for the details).

The alignment of the beams is a multi-step process, which I discuss in greater detail in Appendix A. For the initial alignment through the chamber, we overlap the beams through alignment jigs placed on the flanges that hold the windows. This level of alignment ensures that the laser beams will encounter the molecular beam. Then the lens is placed before the chamber so that the beams are focused in the center.

Our laser beams come to a tight focus, with the beam waist of the 767 nm beam being around 96 μm. A small angular difference between two beams can lead to them being focused in different locations, which would mean that some molecules would

only see one or two of the beams and not the necessary three. To fix this, we created an alignment system that overlapped the beams so that there is an angular tolerance of below 0.08 mrad. We achieved this tolerance by overlapping the beams to about 1 mm over a long-arm pickoff with a total optical length of around 12 mJ.

Similarly, any misalignment of the retroreflecting mirror could cause the 767 nm beam to be focused in a different place on the return trip from the initial focus. In particular, the retroreflection needs to be aligned to better than 0.1 mrad, and we reach this level by aligning the beam into the optical isolator over a long path length.

3.6 Time-of-flight mass spectrometer

At this point in the experiment, molecules that were excited to the higher vibrational level have been dissociated, but we still need to find the proportion of atomic oxygen ions to molecular oxygen ions. Since these have different masses, we can use a time-of-flight mass spectrometer to differentiate between the atomic and molecular oxygen. In the past year, a former thesis student, Boran Kuzhan, made substantial improvements to our detection system [26].

The ions are created between two electrodes in the Wiley-McLaren configuration to give them an initial velocity towards our MCP (Micro-Channel Plate detector, Jordan C701). Refer to Figure 3.4 for these locations, relative to the rest of the apparatus. Then, another electrode gives the ions a further push and, most importantly, helps to focus the ions in time due to a Wiley-McLaren configuration [50]. These three electrodes are the first three plate electrodes in Figure 3.8 (1-3). This configuration allows for enhanced focusing in time, which ensures that particles of the same mass all arrive within a short amount of time ($\sim$40 ns for O_2^+) of each other, regardless of their initial position and momentum state [50].

The ions are spatially focused on our detector by an Einzel lens, also seen in

1	Push Plate	1741 V
2	Grid Plate	1500 V
3	Top Plate	0 V
5	Middle Einzel Lens Electrode	1040 V
4 & 6	Outer Einzel Lens Electrodes	0V

Table 3.1: The recommended, and actively used, voltage settings for the Wiley-McLaren Electrodes and Einzel Lens. Numbers in reference to Figure 3.8. Values courtesy of Boran Kuzhan [26].

Figure 3.8 (electrodes 4-6). The voltages on these electrodes and the lens can be adjusted to optimize our detection [26]. The settings that we actively use are given in Table 3.1.

One important note is that, if the electrodes are left on, the molecules might be accelerated out of the beam waist before all three lasers drive each subsequent transition. In particular, for our calculated beam waist of $\geq$ 96 μm, our voltage difference of 241 V between the grid and push plates will accelerate the molecular ions out of the beam waist in 61 ns. To mitigate the loss of ions, we run the experiment with the plate electrodes grounded and then pulse them on when the experiment is complete.

Overall, the goal of the Einzel lens is to focus the ions spatially on the MCP for enhanced detection [26]. Otherwise, we would be cutting into our signal by simply missing a number of the ions created. The Wiley-McLaren configuration focuses the ions in time, meaning that ions of the same mass arrive at the detector within roughly the same amount of time, regardless of initial position and velocity.[1] This allows for greater confidence in distinguishing between ions of different masses.

[1]Strictly speaking, this time-of-flight mass spectrometer distinguishes mass to charge ratios. Our ions of interest are singly ionized and so we discuss the mass spectrometer as distinguishing between masses.

3.6.1 Detection

Now, we need to understand what the signal from the MCP actually is and how it is interpreted.

The signal from the MCP is a current pulse that we feed into an amplifier, and ions appear as dips in this signal. This amplified signal is fed to two oscilloscopes, with one example trace seen in Figure 3.9. One is the primary oscilloscope to handle our data acquisition. This is the PXI-5152 and communicates directly with the computer. The signal also goes to a RIGOL oscilloscope which has a separate display, useful for working on our setup, but does not communicate quickly enough with the computer. We run the experiment at a rate of 10 Hz. Note that this requires using the Time-Interleaved Sampling property of the oscilloscope with the LabView program (this oscilloscope has 1 GS/s on one channel, but we wish to run at 2 GS/s).

In our LabView program, which runs the experiment (from managing triggering to data processing), we detect dips in our time ranges (or 'time-bins') of interest. If the signal dips below a certain threshold (essentially a reasonable enough threshold to both avoid noise and count all real dips, currently set to -0.1 V), we count that dip as an ion. However, as one may see in Figure 3.10, one shot may have several dips. We track the amount of ions created in two different ways: 1) the fraction of shots with ions and 2) the value of the integrated dips. For the latter, we integrate the dips (starting a couple points before and ending a couple points after the first threshold detection) in order to get a number which better reflects the amount of ions detected. Both of these values are recorded so that we both have the fraction of shots with ions *and* the integrated dips.

Our program is not calibrated to relate an integral value to an *exact* number of ions. However, we expect the integrated molecular ion dips to scale linearly with the number of ions created.

For this thesis, much of the data I will show later are scans showing integrated

ion dips versus frequency over some frequency range. In these cases, the 'ion dips' value plotted is an average over (usually) 100 shots. Thus, the integrated value from the ion bin of interest is averaged over the number of shots taken. That averaged integral is then the one actually plotted. By averaging, we can increase our statistics and somewhat cut down on noise.

3.6.2 Calibrating the mass spectrometer

In order to know which time bins we should be looking for oxygen atomic ions in, we calibrated the time-of-flight mass spectrometer. First, we intentionally clip light on the electrodes by translating the lens. This light causes a large dip to appear in the signal from the MCP. This signal shows the electrical delay in the signal from our spectrometer and so gives a time-offset for the spectrometer. Next, we look at the next significant dip in the signal. This dip is hydrogen (actually protons, because it is ionized hydrogen) and so corresponds with $m = 1$.

Furthermore, we are be confident in choosing our time-bin for the oxygen molecules $m = 32$ because we both see consistent signals there with the oxygen gas on and have seen REMPI spectra consistent with theory for oxygen molecules. Thus, subtracting the offset from the times for H^+ and O_2^+, we used these points to calibrate the spectrometer and so calculated the arrival time for O^+ to be $\sim 4.07\ \mu s$.

For better detail on the dynamics of the molecular beam and work towards photoionization, see [10]. For a good overview of our theory on our REMPI scheme and the two-photon transitions, see [5] and [20] and our brief discussion and citations in Chapter 4. Our new Wiley-McLaren configuration and Einzel Lens design and data are discussed in [26].

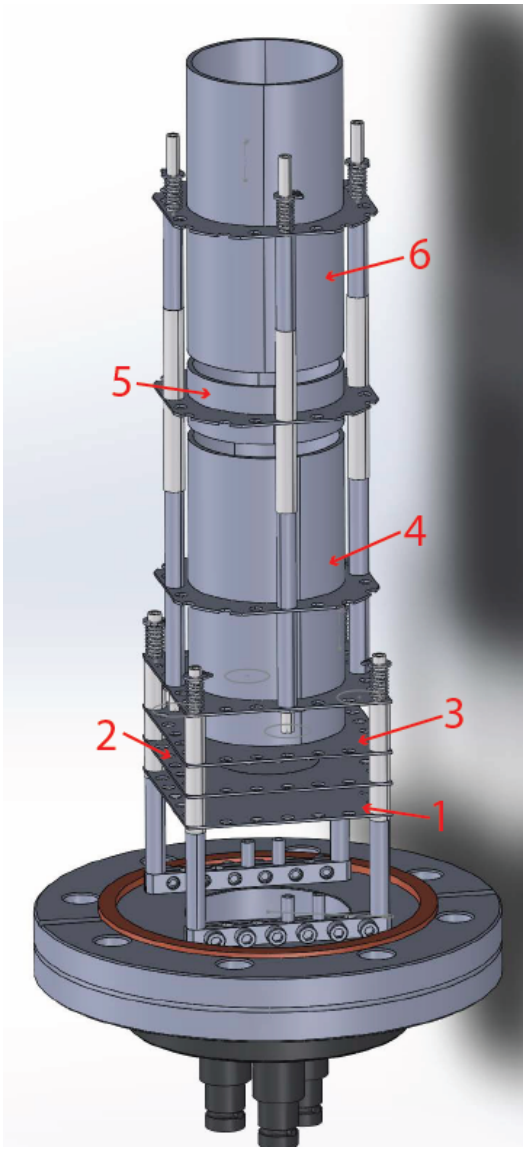

(a) CAD drawing of our electrodes. Courtesy of Boran Kuzhan [26].

(b) Picture of our electrodes before inserting in the vacuum chamber.

Figure 3.8: Here is the electrode setup, including the Wiley-McLaren configuration (plate electrodes 1-3) and the Einzel Lens (cylindrical electrodes 4-6). The "experimental region" where the transitions are driven is between plate electrodes 1 and 2. The numbers also refer to the voltages listed in Table 3.1. The long, cylindrical electrodes are 3" long and the plate electrodes are 2" wide.

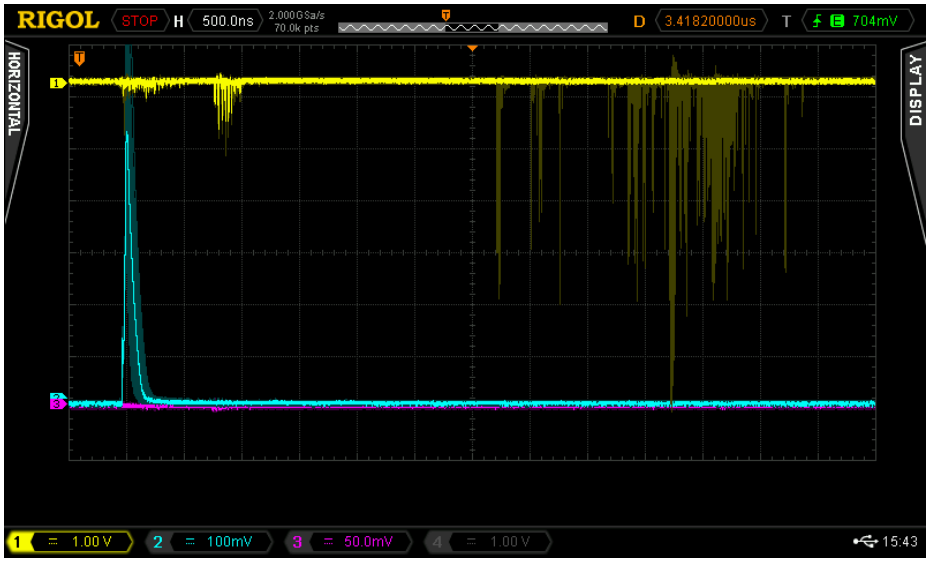

Figure 3.9: The yellow line is an example trace of our signal from the MCP, after amplification. Each dip in the yellow trace represents where we have detected an ion. The deepest dip is where the molecular ions show up. The blue line is the signal from our photodetector, which detects a portion of the laser beams.

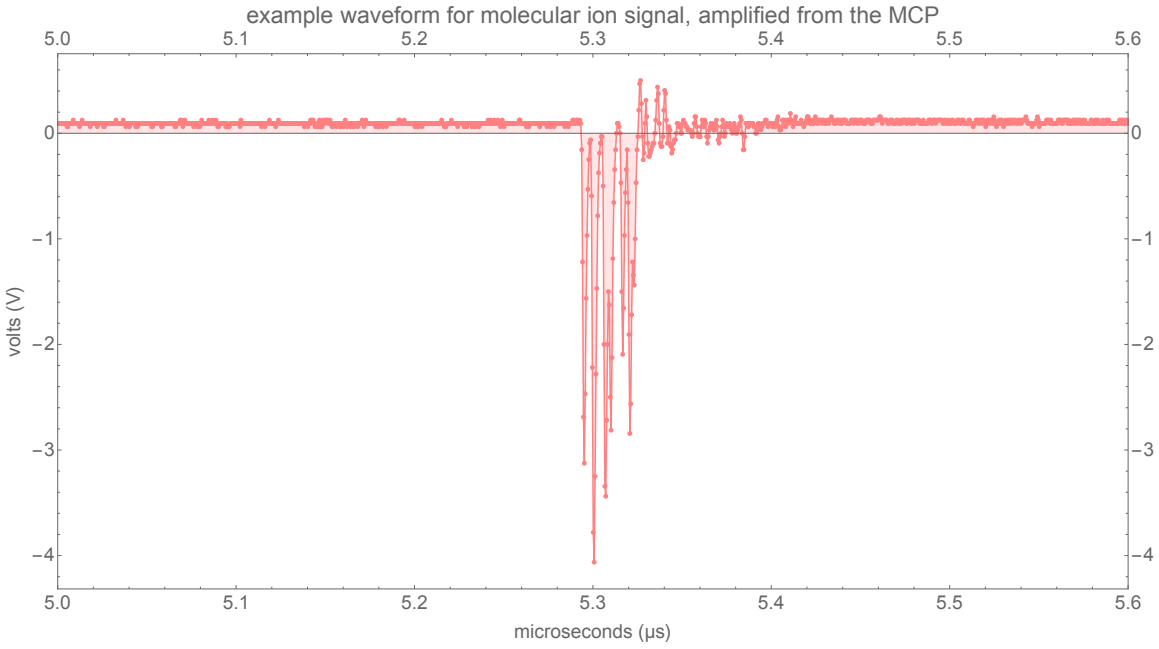

Figure 3.10: This waveform shows the dips in the molecular ion time-bin (with times as shown on the RIGOL oscilloscope). We set the cutoff for an ion detection at -0.1 V. If we detect a signal below that, we count an ion and integrate the dip. The signal seen above is for a typical shot in the molecular-ions time range.

Chapter 4

Experimental Progress and Results

Through work on the apparatus, we have been able bring together the different parts of the experiment and run our first real scans looking for the two-photon vibrational transitions. In order to do this, we first characterized the molecular beam in order to make an educated choice of ionization wavenumber. By scanning the ionization frequency, we determined the temperature of the beam at different points along the gas pulse. This allowed us to optimize the relative timing of the gas and laser pulses to get high rates of ionization from low rotational states. Further, an important part of our detection is dissociation and so we have done calculations to estimate the probability of this dissociation. However, we still have uncertainties to deal with for this step of dissociation.

Our frequency scans looking for the vibrational transition have not yet resulted in any definitive peaks. Issues with one of our lasers somewhat impaired our efforts to drive these transitions. Additionally, we discovered some surprises, such as the ability of our infrared laser to ionize neutral oxygen molecules with eight photons.

These confounding factors and surprises point the way for future improvements to improve the reliability of our experiment and to see the vibrational spectrum.

4.1 Characterizing the Molecular Beam

In order to drive our transition of interest, we need to ensure that our state preparation is working reliably and that it is well characterized. For us, characterizing the beam meant gaining a solid understanding of the gas pulse, especially the temperature. This understanding allows us to choose the optimal delay and duration of the gas pulse. Better estimating the beam temperature further allows us to choose an ionization wavenumber that will ionize the oxygen molecules into the correct initial rotational states.

4.1.1 Gas Pulse Duration and Delay

The timing of our experiment is essential to ensure that the molecules 'see' all three beams for the different transitions. Adjusting the timing also allows us to control which part of the molecular beam we are ionizing. The gas pulse takes significantly longer to travel through the experimental region than the laser does, which makes sense given that the speed of light is relatively high. Because of this, we can tune when the gas pulse arrives at the experimental region relative to the laser pulse, which allows us to select which portion of the pulse we wish to ionize. The gas pulse itself is not entirely uniform. Therefore, we must tune our parameters to optimize our state preparation.

Specifically, we can tune the gas pulse delay and the pulse duration. Increasing the duration allows more gas into the chamber, which is helpful up to a point. While we certainly want a large number of molecules, if there are too many they begin to bounce off of each other as well as the sides of the vacuum chamber and increase the temperature of the gas, which ultimately cuts into our population in the ground rotational states.

In Figure 4.1, we recorded our molecular ion signal with the REMPI laser tuned

to a cold peak, scanning over gas delays for three different pulse durations. This allows us to better understand the shape of the gas pulse, and how it changes for different durations. Using this, we can choose a gas pulse delay so that we are ionizing molecules from a particular part of the pulse.

In these scans, we can see that the pulse shape is especially clear in the low duration scan. The higher duration pulse seems to have a trail of gas behind it. Given these scans, we came up with a rough model for the temperature of the gas: the actual pulse (the peak, like what is most visible for the 110 μs duration) is cold and then it is followed by a warmer trail of molecules.

When we carried out a gas delay scan with the REMPI laser at a hot peak, we found that the ion count stayed low until *after* the initial gas pulse. This finding supported our theory of a cold pulse followed by a warm, diffuse gas.

With this model, we then carried out REMPI frequency scans, whose spectra depend on the temperature of the beam, to test our understanding. Given the initial scans, we were leaning towards choosing to run our vibrational scans with a gas pulse delay of 600 μs and a duration of 130 μs. However, we wished to test the model to be sure that the gas beam was cool enough at those parameters to have enough molecules in the first four rotational states.

4.1.2 Characterizing the Beam Temperature

Confirming our model for the beam temperature was not simply out of interest but actually central to our experiment's success. Because the distribution of states depends on the overall temperature of the beam, we need to have a well-understood beam temperature in order to make educated decisions about which wavenumber to choose for our ionization wavenumber. It is also important to understand the beam temperature so that we know which states we will be ionizing into.

Previous calculations based on the pressure differentials would predict that we

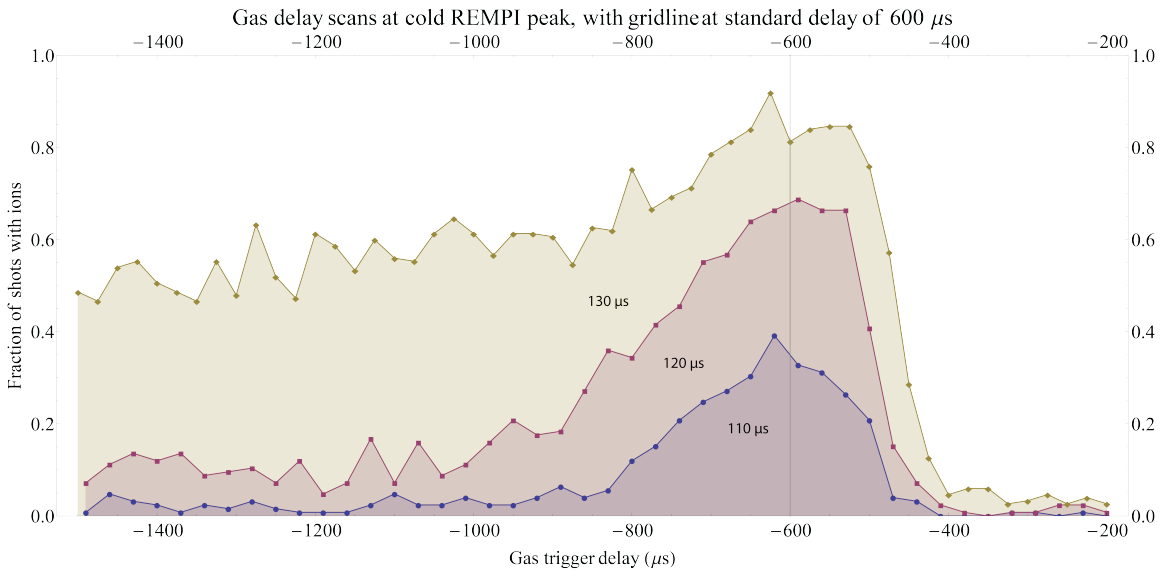

Figure 4.1: Here are the gas delay scans for three different pulse durations, ionizing at a cold peak (16591.0 cm^{-1}): 110 μs, 120 μs, and 130 μs. We can see the shape of the pulse most clearly for the lower durations. The higher duration plot seems to have a trail of diffuse gas after the initial pulse. Moving forward, we are using the 130 μs duration and 600 μs delay. The peak in the 130 μs duration may be an anomaly or it could be due to the valve bouncing, as seen in other similar experiments though on a different time scale [3].

have a gas temperature of around 5 K [10]. However, throughout the past few years, it has been clear that there are some heating mechanisms, which previously lead to a gas temperature of around 300 K. Recent changes, such as reducing the distance the beam had to travel to reach the science chamber and reducing the pulse duration, lowered the temperature of the beam.

Based on the plots in Figure 4.1, we hypothesized that we had a cold pulse of the gas followed by a warmer, diffuse gas. We believed this because, in the gas delay scans at a cold peak, you see a pulse of cold molecules followed by a smaller number of warm molecules. The argument was that these, later molecules might have bounced off of each other, a side of the vacuum chamber, or the valve poppet which might have caused them to heat slightly.

We confirmed our idea by comparing REMPI frequency scans where we intend to

ionize (gas pulse delay of 600 μs and pulse duration of 120 μs) and comparing this to a scan at a higher pulse delay of 800 μs (though at a slightly higher pulse duration of 130 μs) where we expected to have a higher temperature.

Figure 4.2 shows our scan at this longer gas delay overlayed with a theory curve. This theory curve is a calculated spectrum with a rather naive weighting based solely on the population of each energy level from the Boltzmann distribution and the multiplicity of rotational states [16]. Furthermore, these theory curves show the spectrum for the transitions from the $X^3\Sigma_g^-$ ground state to the Rydberg $d^1\Pi_g$ state, both in O_2; the model does *not* include the final transition from the Rydberg state in O_2 to the ground state in O_2^+. So, we cannot expect the spectra to match perfectly, but they are close enough to estimate the temperature.

We can see that the data seem to match the peaks from the 300 K theory curve reasonably well. A larger number of shorter peaks, as we see in Figure 4.2, indicates a warmer gas. Thus, even though our data are not a perfect match with the rather naive theory, we can estimate the gas beam to be around 300 K. This estimate is enough for our goal here, which is to test our model of the gas temperature before moving forward in the experiment. The higher temperature visible in Figure 4.2 at a gas-pulse delay of 800 μs is quite different from the scan shown in Figure 4.3 at a delay of 600 μs.

This later scan, in Figure 4.3, shows a greater difference between the relative heights of the peaks, which indicates a cooler beam. Even so, only overlaying the 20 K theory curve missed some of the peaks at the lower and higher wavenumbers. To adjust for this, we combined both the 20 K and 300 K theory curves to best match the data. Thus, our model of the gas pulse had to be somewhat adjusted. It seems that there is a mix of warm and cold gas at a delay of 600 μs and pulse duration of 130 μs. Some initial scans at a shorter duration looked cold, but the ion count was significantly lower. Thus, we decided to remain at the gas delay and duration

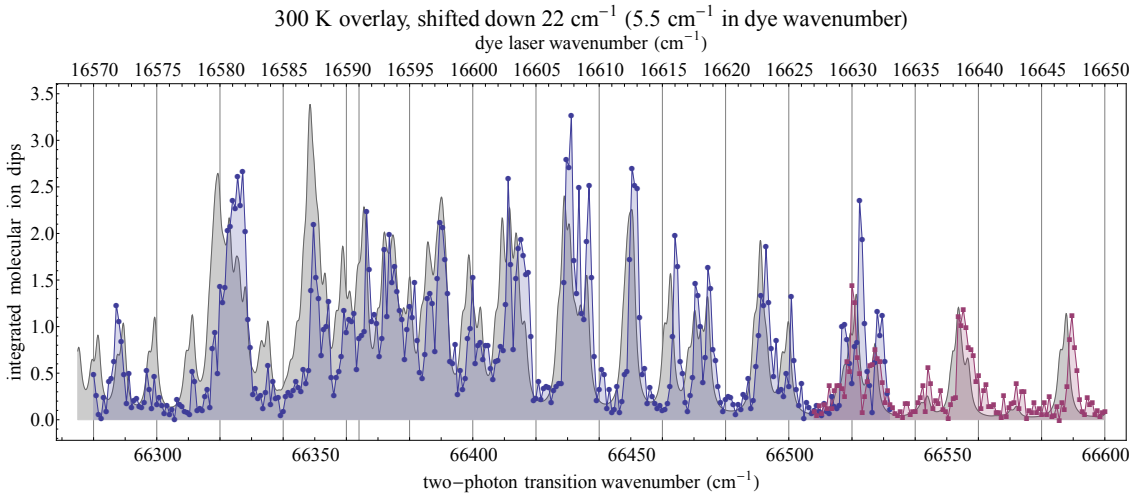

Figure 4.2: Here we see an overlay of our REMPI spectrum (red and blue data) with a 300 K theory plot (gray shaded curve). The beam clearly has multiple peaks of similar height, which indicates a higher temperature. Note that the data was stitched together from two different scans due to issues with our REMPI pulsed laser.

that gave Figure 4.3, especially since, when ionizing at a cold peak, the significant majority of ionized molecules are cold.

Note that, for both of these scans, we have had to shift the theory curve down by 22 cm^{-1}. We do not yet know whether it is our wavemeter or previous values that are incorrect.

4.1.3 Choosing a Peak for Ionization

Now that we have a decent model for the beam, we can refer back to our theory to choose which initial states to ionize into. Looking at Figure 4.4, we see that the molecules are primarily in the N=2 rotational state of the neutral Rydberg state $d^1\Pi_g$ if we continue to ionize at the dye-laser wavenumber of 16591.0 cm^{-1}. It is worth noting that the frequency we chose was based on where we saw the highest number of cold ions. The theory figure might be slightly misleading because it seems that we chose one of the lower peaks at which to ionize. However, referring to our data in Figure 4.3, the peak at 16591.0 cm^{-1} is actually high. This discrepancy in the data

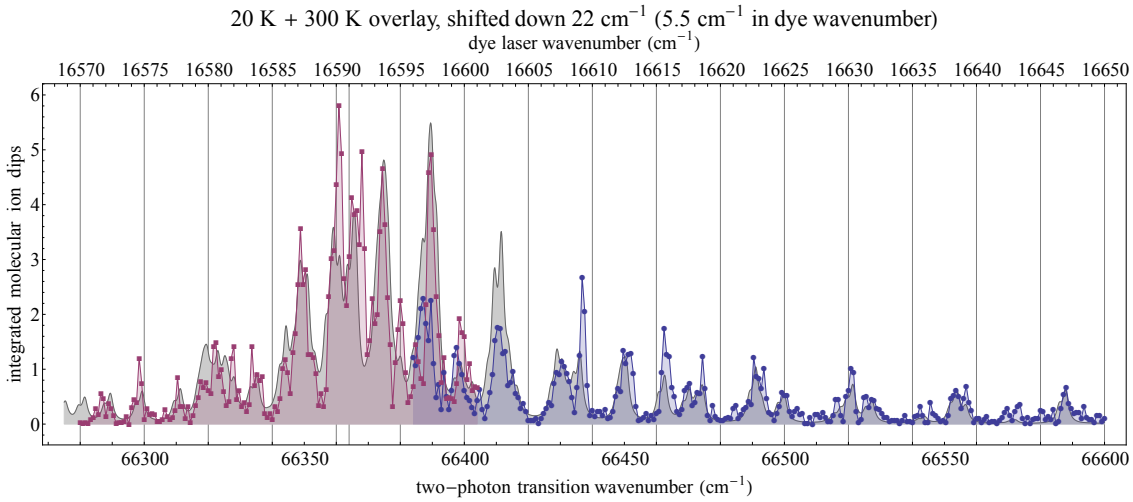

Figure 4.3: This plot shows our data (in red and blue) overlayed with a gray shaded theory curve that represents a combination of the 20 K and 300 K theory curves. In order to get the heights to roughly match the data, we must choose coefficients for each theory curve. The coefficient ratio for the 20 K theory coefficient to the 300 K coefficient was 1:1.4. At the higher peaks, the 20 K beam contributes most of the height. In analyzing this graph, the data shows the high peaks consistent with 20 K as well as other, smaller peaks at higher wavenumbers consistent with around 300 K. The discrepancy in the red versus blue around 16597 cm^{-1} is likely due to our laser warming up slowly.

can be ascribed to the naive method which we use to predict the spectrum.

For the ions that end up in the wrong initial state, which we do expect to happen to some extent, these will contribute to background in our molecular ion production.

4.2 Estimating Dissociation Cross-Sections

As described in Chapter 3, we are able to switch our dissociation wavelength between 266 nm and 355 nm with relative ease. One of the difficulties of our experiment is that, in order to test whether the vibrational 2-photon transition is working, the dissociation must also be working well. Thus, it can be difficult to test these independently. Having some flexibility in our choice of dissociation wavelength can somewhat mitigate this problem.

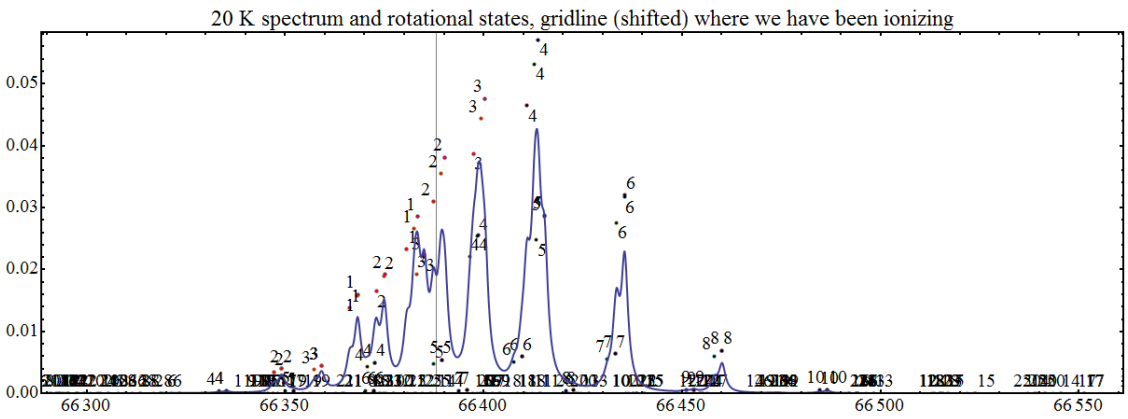

Figure 4.4: Our theory curve for our REMPI spectrum with a temperature of 20 K is plotted with the rotational states for each peak. Our choice in ionization frequency (which, in wavenumbers, is 16591.0 cm^{-1} on our wavemeter) is noted with the gridline. We ionize primarily into the N'=2 rotational state. (The gridline is shifted because of the shift we regularly see on our wavemeter, and so believe to be due to the wavemeter not our experiment.)

Photodissociation (which I tend to abbreviate simply as 'dissociation' throughout my thesis) uses light to drive a bound-to-continuum transition from a molecule in a bound state to a continuum state above the dissociation threshold [5]. In our case, we will be dissociating molecules from the $O_2^+ \ |X^2\Pi_g, v = 16\rangle$ state to above the dissociation threshold in the $O_2^+ \ |1^2\Sigma_u^+\rangle$ state. Because these two states have opposite symmetry (gerade and ungerade), we can drive this as an electric-dipole transition. This means that we can use one photon to excite the transition, so long as the photon has enough energy and there is a good cross-section for that wavelength.

In order to successfully dissociate a molecule, we need to use a photon with at least enough energy to excite the molecule above the dissociation threshold. Our dissociation threshold relative to the ion's ground electronic potential minimum is 54,596 cm^{-1} and, thus, if we subtract the energies of different vibrational levels, we can get the minimum energy required to dissociate an $O_2^+ \ |X^2\Pi_g\rangle$ molecule for any given vibrational level [44]. Most relevant to us are $v = 0$ and $v = 16$. In order to dissociate this molecule from $v = 0$, you need a photon with at least as much energy

as a 186.39 nm photon [16]. For $v = 16$, the cutoff is a 362.38 nm photon [16]. Thus, our two wavelengths of 355 nm and 266 nm have enough energy to dissociate our molecule in the $v = 16$ state but *not* in the $v = 0$ state. We are quite certain about the dissociation threshold.

Even if a photon has enough energy to dissociate a molecule from a particular state, its probability of doing so will depend on the wavefunctions' cross-section. Because the continuum state is a free-state (above the dissociation threshold), the wavefunction is not normalizable, but an asymptotic approximation allows us to calculate the cross-section [28]. For our system, pretty much all vibrational levels had cross-sections that oscillated with amplitude $\sim 0.05 - 0.10$ Å^2, see Figure 4.5.

At this point, the cross-sections are guides to the rates of dissociation we might expect to see. However, we have not cross-checked the absolute values and, as I will discuss later, there are still uncertainties in the $^1\Sigma_g$ potential, which leads to uncertainties in the phase of oscillation. Additionally, while we can relate a cross-section to a Rabi frequency, we have not yet done this calculation for our experiment. We can estimate our expected rate of dissociation by comparing our cross-section amplitude to other similar experiments.

Given work by other labs, we believe that the dissociation should actually be fairly straightforward. For example, one group dissociates AlH^+ molecules with a dissociation cross-section of 6×10^{-22} m^2 = 0.06 Å^2 with a 98% dissociation probability for any single shot [16, 40]. Another group reports a dissociation probability of around 90% for cooled MgH^+ for a single shot [45]. They additionally report low dissociation from other states [45]. Thus, with comparable cross-section amplitudes and laser-pulse intensities, we expect our dissociation to be similarly straightforward.

In Figure 4.6, we can see the effects of our disagreement in parameters for calculating the molecular potentials. Essentially, there are differences in molecular potential parameters for our 'dissociation' molecular potential curve $1^2\Sigma_u^+$ (particularly the

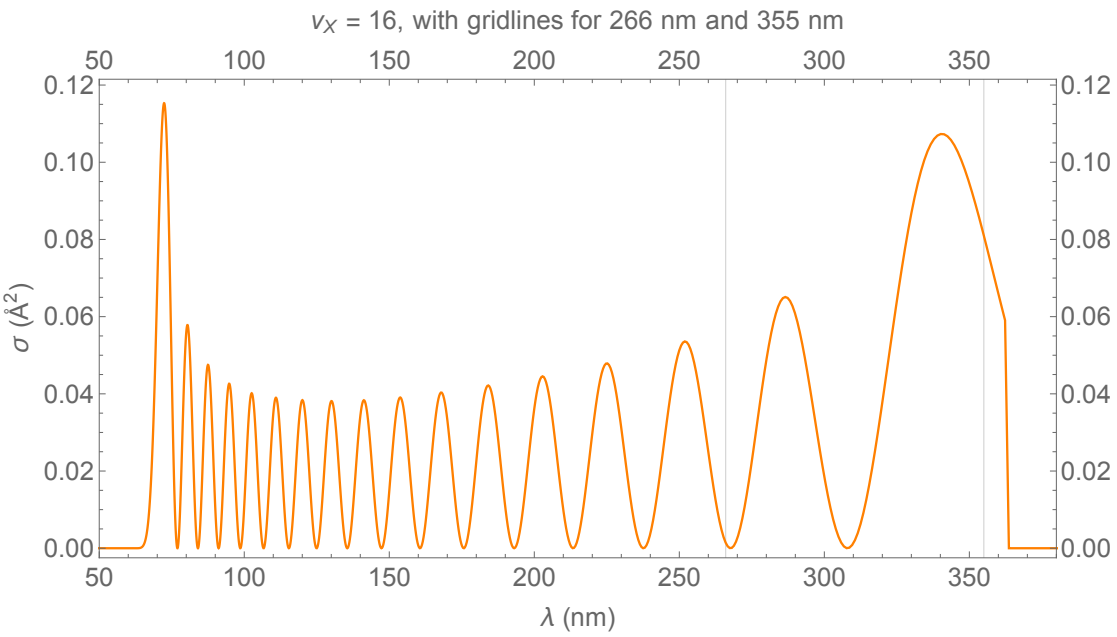

Figure 4.5: This plot shows our estimated cross-section, given in $\dot{A}^2$, for $v = 16$. The two gridlines indicate where our dissociation wavelengths are. While it may seem obvious that 355 nm is the correct choice, there is still reasonable uncertainty about the correct phase for this oscillation and, thus, where exactly the zero crossings are, see Figure 4.6 [16].

depth of the potential, D_e) [4]. We have found disagreements at about 10%, between different papers [16, 29, 8]. These parameters come from different numeric models of the state, which give slightly different values. These parameters are important for determining the location of the potential's steep edge, which is critical for calculating the continuum wavefunction [16]. Thus, our uncertainties about which model gives the correct parameters leads to uncertainty in the phase of the oscillations for these cross-sections.

To better understand the uncertainties in oscillation phase from the different models, see Figure 4.6. Though this figure was made for $v = 15$, the effects of the different models are roughly the same for $v = 16$. While 355 nm would seem to be the obvious choice for dissociation wavelength given Figure 4.5, our uncertainty means that it is helpful and important to be able to test both wavelengths.

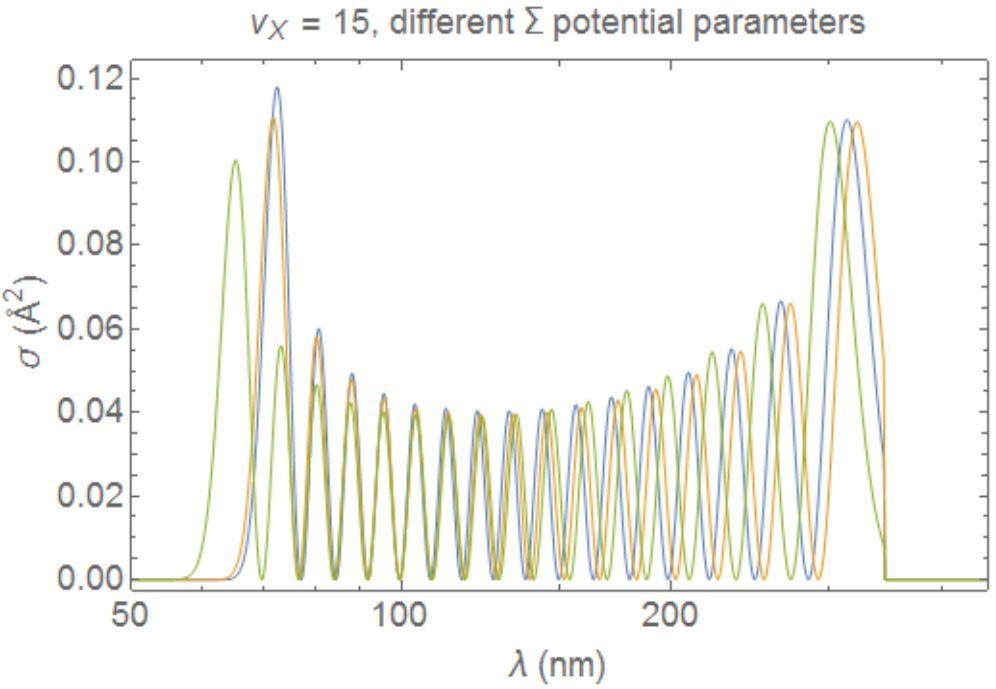

Figure 4.6: We are still some uncertain about the correct parameters for the $1^2\Sigma_u^+$ potential [16]. The different values differ by only about 10%, but, as seen above, these 10% differences in parameters can lead to significantly different zero crossings. Thus, we cannot rely too heavily on the theorized dissociation curves, such as in Figure 4.5. Though this figure is from previous work with vibrational level $v = 15$, the principle holds true for $v = 16$, as well. Figure courtesy of Professor Hanneke [16].

While photodissociation is not the new, scientific goal of our work, we are relying on this step working well in order to get a signal. These uncertainties make our work more difficult because we cannot clearly tell whether the vibrational transition and/or the photodissociation are not working. Having the flexibility in our wavelength somewhat mitigates this problem, though not entirely.

Now, with a better understanding of both the REMPI scheme and the dissociation, we can move forward to a discussion of our first attempts to drive the vibrational transition. I will discuss our current status of the experiments and the results that we have seen so far.

4.3 Attempts at Finding Resonances

A majority of our work this past year involved making some improvement to the system (or fixing something that was broken), then scanning over the range where we expect to see resonances. This thesis represents our first attempts with all parts of the experiment running together, where we might reasonably expect to see the vibrational transitions. Unfortunately, we still have not seen any clear spectrum, but we have achieved clarity on future improvements to make.

I will not detail every step of the process and results along the way, but I will discuss what we have seen in terms of our results for the current state of our experiment. This discussion will be oriented towards what next steps I would take, if I were able to continue work in the lab.

In order to understand what we were expecting to see, I need to first discuss what our criteria for a potential spectrum are. Especially in the absence of any clear signal, there can be small or irregular peaks that look promising to a desperate thesis student. Thus, we must be rigorous in our definition of a real signal.

4.3.1 Criteria for any potential spectrum

In the most naive sense, we are looking for the integrated dips in our $m = 16$ amu range to give a spectrum with clear peaks. In this search, a couple other criteria can help us to be more discerning when analyzing noisy data.

We expect the spectrum to look like the one we have predicted, as shown in Figure 4.7. The theory of two-photon transitions has been worked out by others, and I will not attempt to summarize it here. In my studies, I relied especially on Chapter 5 in [4], [20], and [16] as an introduction to two-photon transition theory in molecules. Other resources I used to learn about two-photon transitions in molecules were [14, 31, 52].

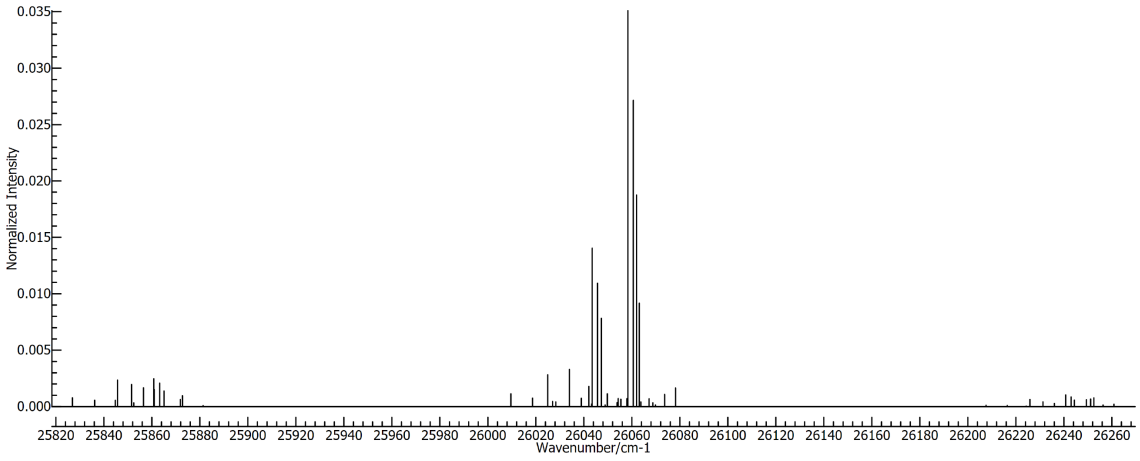

Figure 4.7: This figure was created by former thesis student, Boran Kuzhan, using PGOPHER. It shows our expected spectrum. The three clusters show the three different $\Delta\Omega$ for the transitions. Figure courtesy of Boran Kuzhan, using PGOPHER [49, 26].

To do these calculations, we used PGOPHER, which is an application that can simulate such two-photon vibrational transitions among many others [49, 26]. I will be brief in my description of their calculation method, as the methods are described in [26]. The PGOPHER simulation requires spectroscopic data. Our data was drawn from several sources; a good description of the sources and the techniques they used can be found in [26].

It is still important to note that, in calculating the transitions $O_2^+|X^2\Pi_g, v = 0\rangle \rightarrow O_2^+|X^2\Pi_g, v = 16\rangle$, we assume that our only initial J states are $J = \frac{1}{2}, \frac{3}{2}, \frac{5}{2}, \frac{7}{2}$ because these are the states we photoionize into. Additionally, we made the assumption that the spherical tensors T(0,0), T(2,0), and T(2,2) have equal weight in our calculation [26]. The tensor rank comes from the total angular momentum of the two photons, and we would expect that two photons of the same polarization would combine to rank 0 or 2 [16]. Any further, more detailed, analysis would require a more thorough investigation of the molecule/photon interaction as well as the photon polarization [16].

Additionally, we expect that the vibrational transitions will have a linewidth of

around 0.072 cm^{-1}, set by the bandwidth of our dye laser. The linewidth of the actual transition, which is based on the lifetime of the excited state, is far smaller. So the linewidth we would measure is set by the pulsed laser, rather than the transition itself. We choose to step through the frequency range in step sizes of 0.015 cm^{-1}. This step size would give us around 4.8 points per peak in our spectrum. Thus, any peak we see that is substantially smaller (1-2 points) or larger (5+) is likely not our signal. This consideration becomes important if we use rolling averages to try to reduce noise.

Additionally, if we see any low peaks, we must consider whether those are clearly in the bin with $m = 16$ amu or not. The issue of calibration is discussed in Chapter 3. The molecular ions have an arrive within a time range of less than 50 ns consistently, significantly below the 0.2 μs size of the bin. We would expect similar consistency from the atomic ions.

Thus, if we did see peaks in the time range for m=16 amu, we would first want to check that these peaks were consistent across scans on different days. We would also want to consider whether these were tall (in comparison to the noise) peaks with about 4-5 points per peak. Furthermore, we would really focus on whether these peaks would match the predicted spectrum in Figure 4.7. For further support, we would want to check that the atomic ions arrive consistently within a small time range, like the molecular ions.

Because this spectrum has not yet been seen, having multiple criteria for any possible resonances is necessary. At this point, we have not seen any peaks convincing enough to require the full rigor of these criteria, but developing these criteria has prepared us for when we see the resonances.

4.3.2 Results

So far we have not seen any spectrum that is clearly beyond noise. Even so, there is good reason to think that some small improvements could make a substantial difference and even allow us to see a vibrational spectrum.

While we took scans at every point in the experiment, I will only be showing some of the most recent data, as it represents our system working with all of the changes and improvements.

After characterizing the molecular beam and getting the entire experiment to work together, we took several weeks worth of data with the 355 nm dissociating beam, before switching out the crystals to test the 266 nm beam. There were some significant issues that began to occur with the Quantel Nd:YAG laser that confounded our efforts to see a scan and somewhat negated our recent improvements.

At this point, our results include the various confounding elements of the experiment, as well as some of the unexplained surprises. While the progress made to be able to test our experiment as a whole and search for resonances is significant, these challenges and surprises show the work that we still have to do in order to reach our goal.

I will begin with discussing what kind of data we have seen so far, before moving to focus on some of the major challenges that we can see within these results.

Example data of 2-photon transitions

First, to understand our current progress and challenges, we should consider some example data from trial scans.

We ran many test scans, most of which looked roughly the same, showing noise with no distinct peaks. Scans using the 355 nm dissociation were mostly zero but would have a number of low peaks, with a higher peak every now and then. Re-scanning the same region has not shown any consistent higher peaks. Furthermore,

these initial scans with the 355 nm dissociation were done at every point after our improvements. Comparing these scans from different points throughout the year, has not shown any obvious differences or improvements though it is worth noting that our efforts to improve the experiment were complicated by other aspects breaking.

In the last week of taking data, we switched out the final crystal in the Innolas Nd:YAG to get a 266 nm dissociating beam. First, I want to note that this beam ended up laser-machining a telescope along the optical path, which meant that we had to remove the telescope and just work with a larger beam (and thus a tighter, more easily misaligned focus). Early scans with the 266 nm beam showed atomic ions arriving at nearly the same rate as molecular ions. We have determined this to be background noise and thus lowered the beam energy to mitigate the problem.

Overall, our test scans were noisy and confusing. More sophisticated methods of data analyzing, guided by our criteria, did not show any definitive spectra either.

We have taken many scans over the region in frequency where we most expect to see transitions. The uncertainty for the wavenumbers, given the best available data, is ± 5 cm^{-1}. Thus, we generally scanned our 767 nm laser from 13010 cm^{-1} - 13040 cm^{-1} so that, in our predicted spectrum, we would cover the region of 26020 cm^{-1} - 26080 cm^{-1}, because the transition is a two-photon transition. However, once the photoionization is more reliable, we can begin to scan broader regions more thoroughly.

These two example data sets I show (Figures 4.8a and 4.8b) are both over the same region but are using different dissociation beam wavelengths. Note that this difference required us to adjust the energies. When using the 355 nm beam (Figure 4.8a), the dissociation beam had an energy around 15 mJ. To mitigate the background from the 266 nm beam, we turned the energy down to 3 mJ but may have to go even further.

In these frequency scans, there are no clear peaks. Comparing the two, the data in Figure 4.8b (for 266 nm dissociation) are generally higher than the data shown in

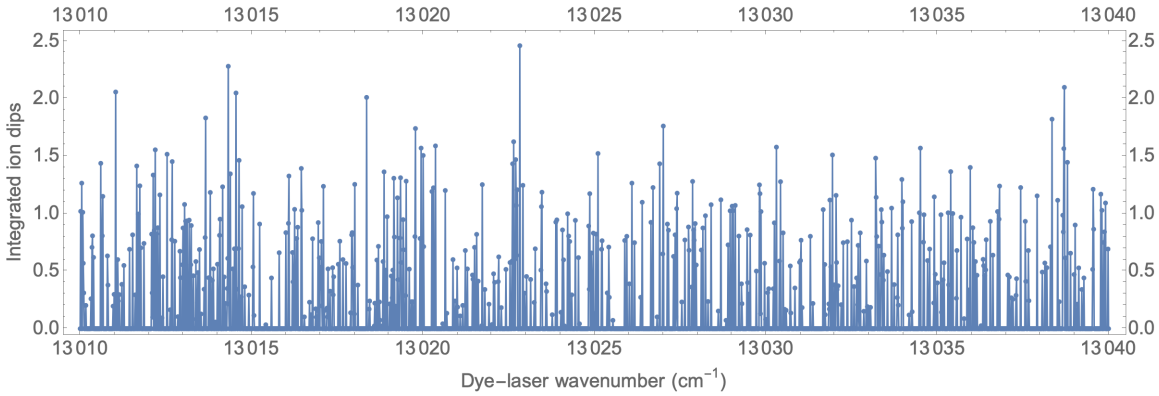

(a) Example data for 355 nm dissociation wavelength, with laser energy at 15 mJ.

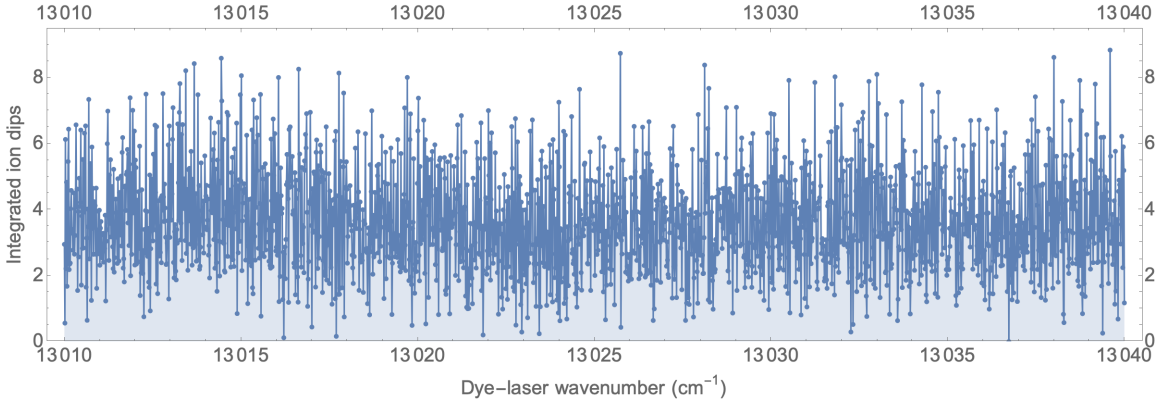

(b) Example data for 266 nm dissociation wavelength, with laser energy at 3 mJ.

Figure 4.8: These two scans both show results from a frequency scan of the vibrational beam from 13010 cm^{-1} to 13040 cm^{-1}. Both are on the same scale and show the (re-scaled to be 10^{-10} V·s) integrals of the ion dips from the narrowest time-bin where we expect to see O^+. We can see that the 266 nm dissociation beam created significantly more atomic ions, but there is still no clear signal. In both cases, the scans show noise that stays relatively constant throughout the scan. The complete set of plots for different time bins for each scan can be seen in Appendices C and D.

Figure 4.8a. It is difficult to know quite how to interpret this. Our goal in changing dissociation wavelengths was to make dissociation more likely, which would increase our signal. However, at higher energies, we clearly saw that the 266 nm beam was adding significantly to the background. At this point it seems that the increased integrals might be due to background, but I cannot say definitively.

Another unexplained issue is that in both scans (Figure 4.8) the O^+ signals do not seem to depend on the molecular ion creation. For example, compare the relative stability of the integral in Figure 4.8b with declining molecular ion creation, shown in

Figure 4.9. Similarly, the ion production is low but relatively constant for the 355 nm dissociation scan in Figure 4.8a but the corresponding O_2^+ production is not constant (refer to Appendix C for the plot). To this point, we have not seen any indication that these signals (the O^+ and O_2^+) are correlated, beyond noting a drop in the O^+ rate if any of the lasers are turned off. The one notable exception is our run with the 266 nm laser at 15 mJ. The O^+ and O_2^+ signals had the same shape, though no peaks were present. However, in this case the molecular ion production was highly dependent on the 266 nm dissociation beam *not* the REMPI 301 nm beam. Thus, we have no reason to believe that the molecular ions were in the correct initial states. Therefore, I feel reasonably confident in saying that we have not seen any atomic-ion signals clearly dependent on the REMPI molecular ion production.

While these data might leave us with more questions than answers, the initial scans can provide a starting point, and we have found several clear issues along the way that can help to guide future work.

Issues with the Quantel Nd:YAG laser

Even though we have scanned this region in frequency many times with different parameters, I cannot say that our experiment would not work with these parameters because the molecular ion production was significantly deteriorating. For example, when acquiring the data I present in Figure 4.8b, we had poor molecular-ion production, shown in Figure 4.9.

The DMO option (discussed in Chapter 3) means that, even if the laser is nominally on resonance with a peak, the axial modes will only be on resonance with our transition about 10% of the time. Thus, towards the end of this scan, with a generous estimate of 20% of shots containing molecular ions and only 10% of these shots happening while the axial modes are on resonance, only 2% of the shots could successfully make the transition. Even this estimate assumes that the dissociation

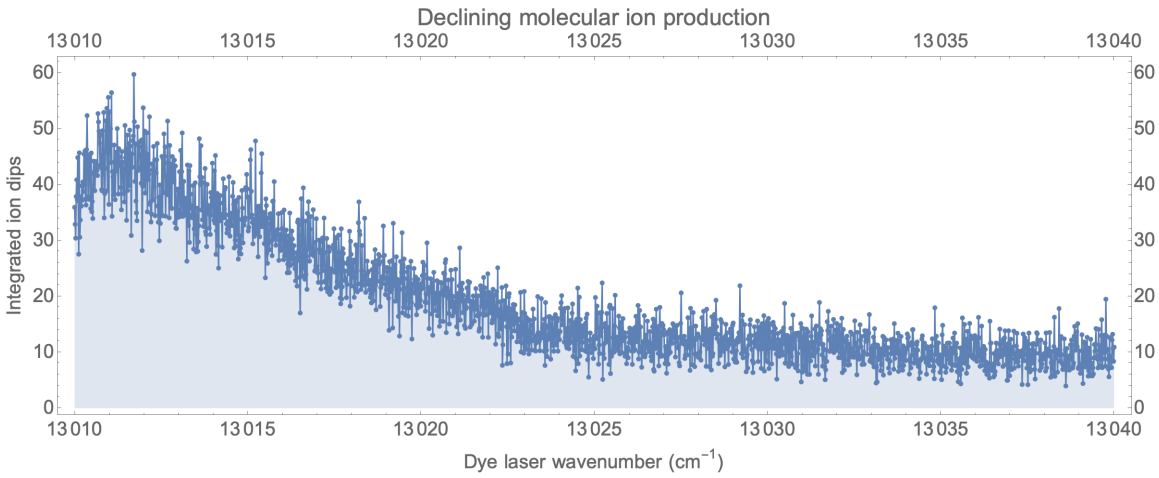

Figure 4.9: This figure shows the integrated dips for the scan showed in Figure 4.8b. Here, we see that the quantity of ions produced significantly declined over the course of the scan. The fraction of shots with ions began at around 50% and ended at around 20%.

works perfectly. Given time constraints and our need to have small step sizes, we ran these scans with 100 shots per point. Thus, we would only expect to have two shots from the total work for any point, which severely limits us in terms of getting a decent signal-to-noise ratio.

It is worth noting that the ion fraction is *not* necessarily the number of ions created in each shot; it is the number of shots with ions. Thus, in one shot with an ion, we might actually be getting several. So, when I say that we would get about two shots where the experiment could work, that does not mean that we would only have two resulting atomic ions. We could have several more ions, which does help our signal to noise somewhat. Regardless, in the processed data, one shot with multiple ions will still only show up as one high point, which is difficult to trust as a legitimate signal.

Note also that, due to background photoionization by the 266 nm or 767 nm beam (both of which we have seen) there are actually fewer than 20% shots with molecular ions in the correct initial state. In particular, at these energies for the 767 nm and 266 nm lasers, I found (blocking the photoionizing, 301 nm beam) about 2-3% of shots had molecular ions. Because these molecules are being ionized through mechanisms

we do not understand, we have no reason to believe that they will be in the correct initial states. Thus, relative to only 20% of shots with ions, a non-negligible amount are in the incorrect state and, therefore, are not actually useful to our experiment even though they are counted in the molecular ion data.

Furthermore, these estimates ignore the other ways that we might lose a molecule to the experiment, even if it was excited into the correct rotational state in O_2^+ $|X^2\Pi_{g,\frac{1}{2}}, v = 0\rangle$. For example, as discussed during the achromatic lens section, the beams may not be perfectly focused in the same place or overlapped.

These problems emphasize the need for a robust photoionization system, as it is central to the success of our work.

Issues with the achromatic lens

One issue that seemed to harm our signal was our achromatic lens. It was accidentally laser machined the very first time we used it, and so it was never fully tested. The lead time on the new achromatic lens was long, and so it has not been able to arrive and be replaced yet. I argue that the effect of the achromatic lens being machined can be seen in Figure 4.10. The figure shows a drop in ions within the first few wavenumbers, and this was our first run with the new lens. Thus, when the new achromatic lens is able to be placed, we should see a higher signal and, hopefully, the vibrational spectrum.

We have also seen some significant background where, for example, the 266 nm beam photoionizes oxygen on its own. The tighter focus given by an achromatic lens that is not burnt will increase our signal, but it will also increase some of our noise.

Regardless, in comparison to using a lens that is optimized for particular wavelengths, using the achromatic lens should help significantly because we can be more certain that the molecules will 'see' the vibrational transition and dissociation beams.

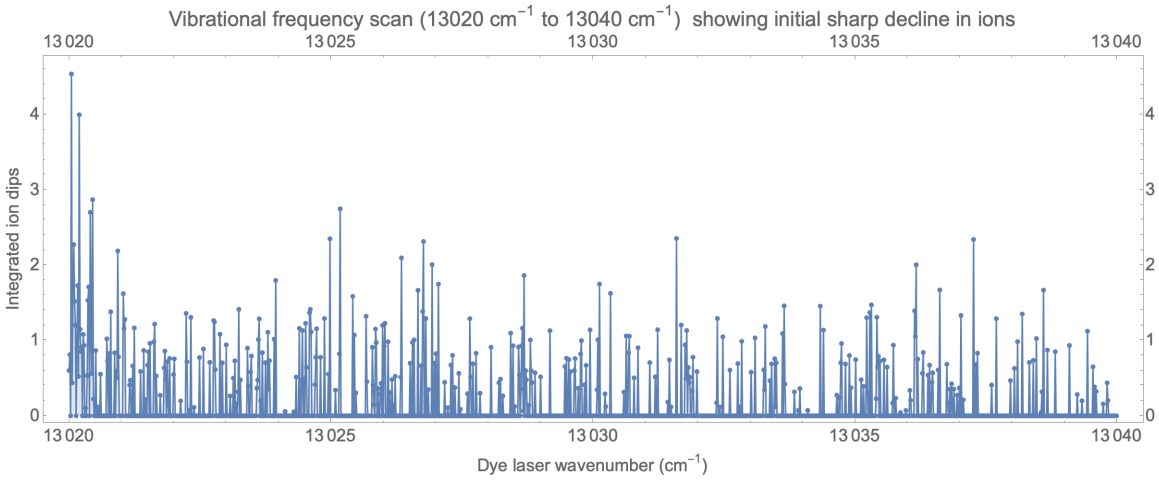

Figure 4.10: These data show the molecular ions in the narrowest time bin corresponding with $m = 16$ amu. Note that we were using the 355 nm dissociating beam here. There is a clear downward trend in the beginning, which I argue is due to the achromatic lens being laser machined. Otherwise, there are a couple peaks but no clear spectrum.

4.4 Surprises

During our work, we found some other surprising results that may give us some insight into our experiment. I will discuss the most notable surprises, in terms of significance to our experiment and my general interest in the surprise.

4.4.1 Mystery Signal

One feature of our system, which we are trying to understand, is a strange signal that has to shown up in the 5.52 μs - 5.92 μs time bin (which corresponds to a mass range of $m = 37 - 44$ amu). This signal depended on the 767 nm vibrational beam, meaning that by blocking lasers we found that the signal appeared with the 767 nm beam. Additionally, it is highly dependent on intensity, since the signal disappeared when we blocked the retroreflection and would die out throughout a scan.

The actual meaning of this signal remains opaque. The spacing of the peaks in our figure below is 1 cm^{-1}. However, there are no obvious molecules or atoms in this

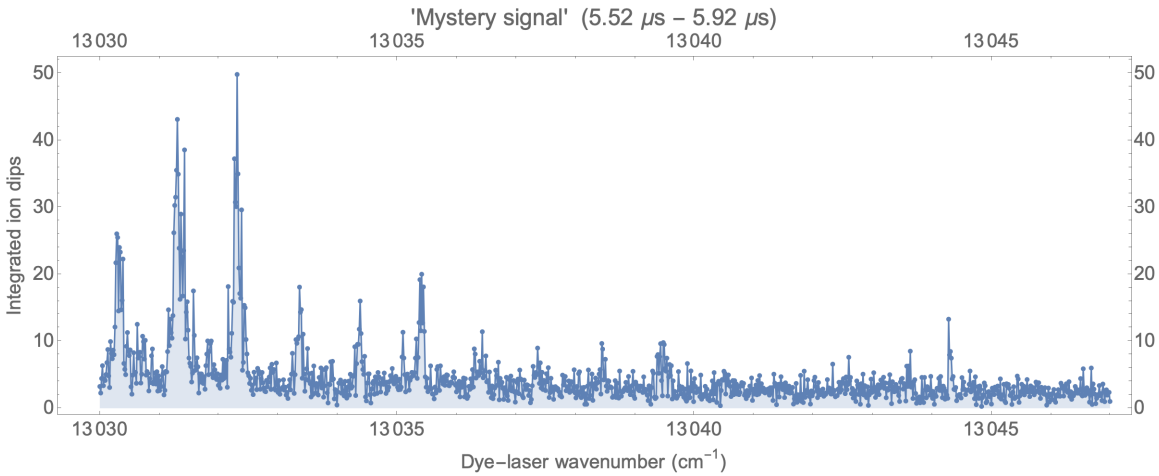

Figure 4.11: This plot shows our mystery signal. There seemed to be resonances or oscillations in this particular time bin, associated with masses in the 38-40 amu range. In spite of an interesting signal, we have not gained any further clarity. In particular, some conflicting data from this same time bin can be seen in the "bin 4" plots from Appendices C and D.

range that have accessible transitions around these energies. Additionally, the signal does not always appear, and when it does the data seem to conflict with each other with some scans showing resonance-like peaks (Figure 4.11, others showing a small blip of signal (in Appendix C), and other scans showing only noise (in Appendix D).

I mention this signal partly due to personal interest. It is always exciting to learn more about a confusing signal. Additionally, at this point of uncertainty in our work, it is useful to try to characterize the system as fully as possible, so long as these tangents do not take away from the primary goals too significantly.

4.4.2 Photoionization with infrared light

One particularly surprising result we observed is photoionization with only the 767-nm vibrational laser. When we blocked the other lasers, leaving only the 767-nm beam and ran the experiment for one minute, we saw the persisted trace on the oscilloscope, shown in Figure 4.12.

Note how, in Figure 4.12 which shows all dips (sometimes overlapped), the dips

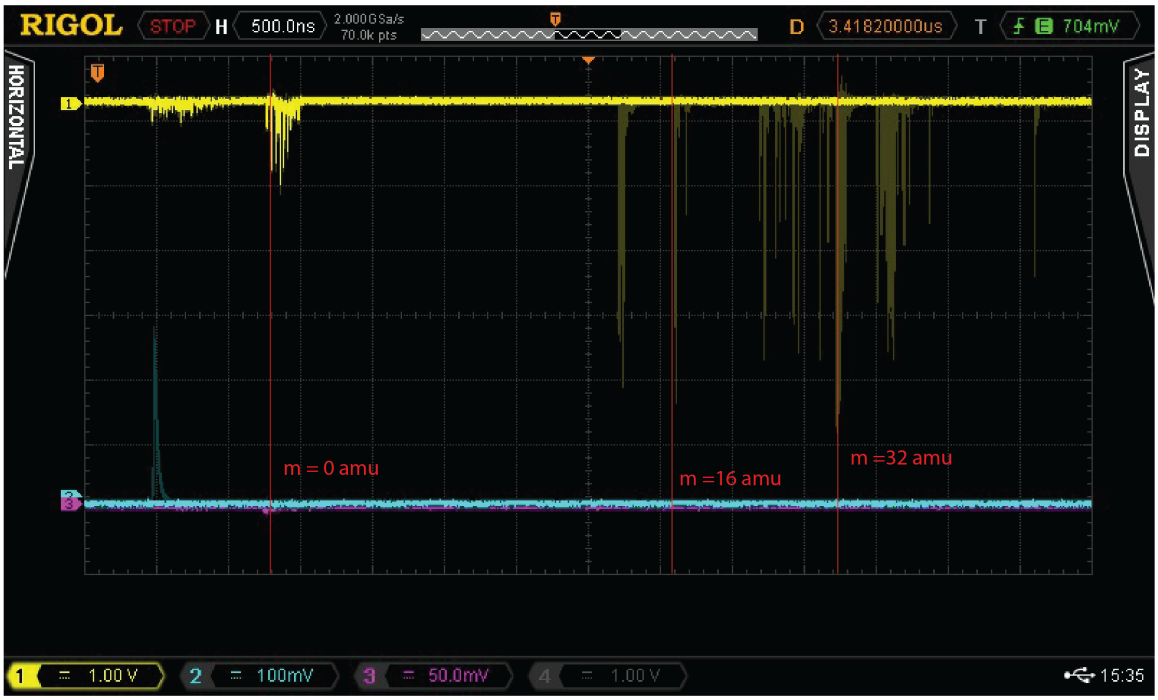

Figure 4.12: This image was created by running the experiment but blocking every laser *except* the 767-nm infrared laser. We let the experiment run for a minute to collect the dips on the oscilloscope, which is shown above. I have indicated where the different, relevant masses are using a scale created with the full experiment running and referencing m=32 amu to m=0.

at m=32 amu are prominent. This image is not weighted by how frequently the dips appear, and some of the contrast between prominent and weak dips is lost. Thus, if ions appear continually in the same region, they may not be visible in the figure. Even so, the dip at m = 32 amu is prominent. While our molecular-ion production rate was certainly not as high as with the 301-nm photoionizing beam, we got a surprising rate of molecular ions with just this infrared beam.

In order to reach the ground electronic and rovibraitonal state in the ion, we need the energy of just under three 301-nm photons. Thus, significantly more infrared photons would be needed to ionize these oxygen molecules. We found one group that did multi-photon ionization of air, enabling them to find 8-photon transitions

in oxgyen with an infrared laser at 800 nm [41]. So, such transitions have been seen before, but they require a high number of photons. Also, it is unlikely that this transition with infrared photons is resonant.

Given that this transition requires many photons and is likely not resonant, it seems highly unlikely to occur.[1] What is surprising to me here is that we could see (likely) non-resonant, 8-photon infrared photoionization but not a resonant, two-photon transition. This unexpected result has led me to question our dissociation method, as it seems unlikely that the infrared photoionization would occur but a resonant, two-photon transition would not.

Ultimately, seeing the photoionization with the 767-nm beam does *not* mean that the 2-photon vibrational transition is being driven. We will not know that we are successfully driving the transition until we see the resulting spectrum. However, it does lend some credence to our belief that it is reasonable to expect to see a vibrational spectrum.

4.5 Discussion

In Chapter 2, I discussed some of the many advantages of using a molecule. These absolutely remain true. Yet, in this current chapter we see some of the difficulties of using a molecule as well. The many degrees of freedom allow us to drive narrow transitions with higher sensitivity to changes in μ, but these degrees of freedom also lead to a multitude of states that leads to unexpected transitions being possible.

These narrow transitions also require high-intensity beams [5]. However, these high-intensity beams (i.e. pulsed lasers with a reasonable energy) can further amplify some of the unexpected transitions, such as the photoionization with the 767-nm beam or the high rates of photoionization with 266 nm! This high intensity can

[1] In particular, the lab which carried out the 8-photon photoionization calculated a cross-sectional area of $\sigma_8 = (3.3 \pm 0.3) \times 10^{-130}$ $\mathrm{W}^{-8}\mathrm{m}^{16}\mathrm{s}^{-1}$ [41].

furthermore cause technical issues. We (accidentally!) laser machined several lenses along the way, particularly our achromatic lens. Thus, these high intensities, which in general make our experiment more likely to succeed, can pose unexpected roadblocks by increasing the background noise.

The question of dissociation wavelength remains open. Though I spent a week running scans with the 266 nm dissociation beam, I cannot say that we have fully tested this dissociation wavelength, as the REMPI laser was doing so poorly that week. Seeing photoionization with the 767 nm beam seems to suggest that, if we can drive a non-resonant transition requiring something like 8 photons, we ought to be driving a resonant, 2-photon transition. Yet, we have not seen the predicted spectrum. Thus, we must test the dissociation wavelengths more thoroughly. Our difficulty here is that the dissociation ought to be straightforward, but we have not seen any signal. We now face the problem of trying to increase a signal that does not clearly exist yet.

Furthermore, regardless of the difficulties and advantages of our experimental design, our recent work has made it clear that reliable photoionization using our REMPI technique is absolutely essential for the experiment to work. With the many parameters of our experiment, it is critical to be as sure as possible about what we *can* control or understand. Once all known parameters are optimized and reliable, we can truly feel confident when running our experiment and comparing data across multiple days.

I do not write all of this discussion of confusing signals and confounding factors to sound pessimistic about the experiment or our work. Rather, I wish to point out that the difficulties and advantages of our experiment go hand-in-hand. On top of the common difficulties of an AMO lab (namely, robust laser systems), using a molecule poses great advantages and creates added complications, which we do not fully understand yet. There are clearly upgrades to be made, the difficulties with our

REMPI laser were mentioned throughout, but we will not know exactly what will be required to see the O_2^+ vibrational spectrum until we have actually seen it. Then, of course, we will have known all along that *this* most recent change was what was needed for our experiment to work.

Even so, in order to *actually* know that whatever most recent change led to our experiment being successful, we would need the rest of the process to be reliable. I will discuss what these thoughts mean more concretely in the following chapter.

Chapter 5

Conclusion

We have been able to bring the experiment to a point to look for these vibrational resonances. Because we have not yet seen these transitions, it is essential to consider what parts of the experiment need clear improvements. I will give some recommended next steps to either improve the experiment or increase our understanding of it. I will also discuss some of the future goals of our work, beyond first measurements of this spectrum.

5.1 Short-Term Goals

The short-term goals follow a couple of basic themes. Most importantly, we need to ensure the reliability of each part of our experiment. Another area that we can work on, in tandem with the issue of reliability, is to decrease the dead-time of the experiment the experiment. Once we are able to scan more reliably and quickly, we can focus on gaining a better understanding of our experiment. I go into greater detail on these themes below.

Our most pressing short-term goal is to make the REMPI scheme more reliable. One way to achieve this is making the Quantel Nd:YAG laser more robust. As much as possible, we should understand how to keep it working consistently so that we

will always be photoionizing many molecules into the correct initial state. We have made some progress on troubleshooting this system. In particular, the temperature control was poor, and we have seen that the output energy was dependent on the temperature within the laser. We are working on a temperature stabilization system, which appears promising so far.

If it seems impossible to get the Quantel Nd:YAG working reliably enough, we could also split off some of the green (532 nm) light from the Innolas Nd:YAG to pump the Quantel dye laser, in addition to the SIRAH dye laser. Because the Innolas laser is working consistently, we would then have a reliable state-preparation system. This solution does have some drawbacks, as it does not allow the same flexibility for pump-beam energies for the SIRAH laser. Additionally, it would require that we manage all of the relative timing for the laser pulses with optical path length. While this is certainly doable, it means that the relative timing will no longer be as easily adjustable. Overall, either of these solutions ought to work and help to ensure that our state-preparation becomes reliable, which is a necessity in order to get decent signal to noise.

Another issue in our experiment is the dead time. We nominally run the experiment at a rate of 10 Hz, and so with 100 shots at each step we should take about 10 s per step. However, we have seen additional dead time (up to around 20% most recently), which can substantially increase the time for each scan. We want to scan over as broad of a frequency range as possible each day, while still going in small enough steps to get several points per peak *and* getting decent statistics for each point. All of the vibrational frequency scans that we discussed during this thesis took about a full workday to get. Any dead time for each point adds up and can significantly slow down our scans, which limits either the statistics or frequency range (or both). I have spent a reasonable amount of time trying to track down this problem, but I do not have any clear answer yet because sometimes the extra dead time has disappeared.

Furthermore, our 767-nm beam energy declines over time due to the declining efficiency of the dye. We should also monitor the energy so that we can normalize for variations. One part of this could be scanning backwards in frequency, since this would reverse the trend. Our laser is designed to scan forwards in frequency. When moving backwards in frequency, the laser corrects for back-latch in the motor. While this is helpful for accuracy, the back-latching adds significantly to the time to run these scans. Finding a way to scan backwards more quickly would also help our signal to noise with two scans (going opposite directions) averaged together.

Given the time (and a more robust state-preparation system), I would have also wanted to do more control scans as well as scans over a wider range in frequency. The control scans would be most useful to do once the photoionization is steady and reliable and after any other major changes have been made. These control scans could both mean scans without any gas pulsed into the chamber or scans with one or several lasers blocked. Especially due to the strange dissociations and ionizations from the 266 nm laser, it would be worth better understanding what background results from just that laser.

Additionally, it would be helpful to do larger scans in frequency once the system was working consistently. During my thesis, we repeatedly scanned the region that was predicted to have the highest peaks in the spectrum (referring back to Figure 4.7). Yet, because we have not yet seen those peaks, we cannot be certain that they are there (additionally, we have a general uncertainty of ~ 5 cm^{-1} for those peaks) [16]. Part of the reason that I think we have not fully tested either dissociation wavelength is that we never carried out these longer scans.

Some other parameters to consider testing and changing are the energies of the 767-nm beam, the 355-nm beam, and, especially, the 266-nm dissociation beam. The 266-nm beam still seems to add to the background signal. So I would want to try to turn down the energy further and attempt a scan at that point.

Furthermore, given the importance of having the DMO option working on the SIRAH laser, we may also wish to have a way to actually see the axial modes. In order to be sure that the DMO option is working, we could build a cavity that is able to resolve these peaks. While the DMO option is conceptually very simple and ought to work easily, it is essential to our experiment. Thus, double-checking this would be an important part of troubleshooting.

In order to measure these peaks absolutely (rather than their relative positions to each other), we would want a better frequency reference than our wavemeter, which has a consistent, unexplained offset. We have worked on a potassium vapor cell but ran into some unexpected challenges, likely due to using a pulsed laser. While less urgent than making the Quantel Nd:YAG more robust, figuring out how to calibrate our wavenumber measurements is an essential step once we have the vibrational spectrum.

Additionally, once we have seen this spectrum, we will need to do substantial work to ensure that we understand it before moving forward in the experiment.

5.2 Long-Term Goals

Once the vibrational spectrum has been seen, we can find more precisely what frequency of light is needed to drive the transition from our 'science state' of O_2^+ $|X^2\Pi_g, v = 0, J = 1/2\rangle$ to our choice of rotational state in O_2^+ $|X^2\Pi_{g,1/2}, v = 16\rangle$. Currently, our measurements of the vibrational transition would be limited by the pulsed laser. Thus, we would need to use a continuous-wave laser.

Most importantly, we will need to carry out the experiment in an ion trap. This trap is essential for cutting down on both our systematic and statistical uncertainties [5]. Furthermore, it is necessary for our future method of state detection using quantum-logic spectroscopy.

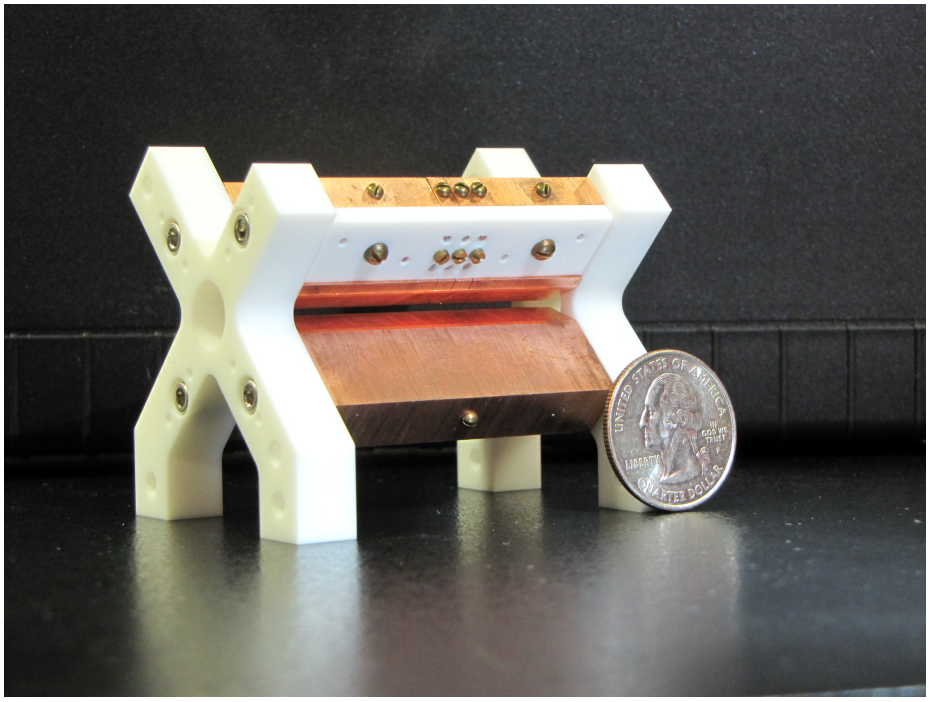

Figure 5.1: This is our linear Paul trap outside of vacuum with a coin for size reference. The four metal bars are electrodes. Two diagonal electrodes remain at ground while the other two oscillate at an radio frequency to trap charged particles [34, 33]. Picture courtesy of Professor Hanneke.

The ion trap itself is a linear Paul trap, Figure 5.1. It uses high voltages, switching at a radio-frequency on the electrodes, to create a potential to trap the ions [34, 33]. We can then carry out the experiments in this trap, before dumping the molecules and ions down the time-of-flight mass spectrometer [33, 26].

Furthermore, in order to get to the lowest motional state in the trap, which is necessary for our level of precision, we will sympathetically cool the oxygen molecular ions with beryllium ions [5, 27]. These co-trapped ions can be used as the 'spectroscopy ion' and 'logic ion' for quantum-logic spectroscopy (QLS), which will allow for state-detection without dissociating the molecules [27, 39].

There is still much exciting work to be done before the eventual result of a highly precise measurement of the change in μ is reached.

5.3 Summary

Throughout our first searches for vibrational transitions, we have found the right region to look for the transitions. We have continually made changes and upgrades to our experiment and have better characterized it. The various parameters such as timing of the laser pulses, the gas valve, and electrode pulses, as well as the electrode voltages have been optimized to increase the chances of seeing these transitions.

While improvements are certainly still left be made, the work that went into understanding where and why the experiment might fail to see resonances should aid these efforts to drive the vibrational transitions. In the meantime, we must not become discouraged, as trying to find something no one has ever seen before is both the most exciting and frustrating part of science.

Appendix A

Details of Spatial Alignment

A.1 Aligning the beams

Because the photoionization and vibrational transitions have transition rates that depend on the intensity of our beams, we need to bring the beams to a tight focus and make sure that all three are well-overlapped in space [5].

In particular we want to be sure that the beams are able to be aligned well enough that they overlap at the focus. The radius of the beam at the focus is referred to as the beam waist and is given by

$$\omega_0 = \frac{M^2 \lambda f}{\pi \omega_L},$$

where M^2 is the propagation constant ($M^2 = 1$ for Gaussian beams), λ is the wavelength of the laser, ω_L is the collimated input waist (or the size of the beam before it is focused), and f is the focal length of the lens. Note also that this equation does not include spherical aberration. Taking this into account would relax the focus and, thus, our constraint.

So, for each beam, we can find the beam waist. In order to find out how well they can be overlapped, we need to know the displacement of the beam waist in the focal plane. Then, we find how misaligned the angle of the incoming beam can be where

Laser	Wavelength (λ)	Beam Radius (ω_L)	Tolerance (θ)
REMPI	301 nm	1 mm	0.10 mrad
Vibrational beam	767 nm	2.5 mm	0.10 mrad
Dissociation 1	355 nm	0.6 mm	0.19 mrad
Dissociation 2	266 nm	0.6 mm	0.14 mrad

Table A.1: Our calculated angular tolerance for each beam given by the beam parameters and Equation A.1. Our long-alignment arm can reach an alignment at least as good as 0.08 mrad.

the beam waists are still partially overlapped. The focal plane displacement is

$$y = f \tan\theta \approx f\theta.$$

Thus, if we want $y < \omega_0$, then we get an angular tolerance of

$$\theta < \frac{M^2\lambda}{\pi\omega_L}. \tag{A.1}$$

For all beams, we (incorrectly) assume that they are Gaussian and so $M^2 = 1$, as opposed to some higher value. While this is incorrect, it gives us a tighter constraint and so, if we meet the angular tolerance with this assumption, we will certainly be overlapped for our actual beams. For an overview of these equations for any students, see [42].

Given the angular tolerances outlined in Table A.1 based on our beam parameters, the beams must be overlapped to at least around 1 mm over 10 m. In order to address this problem, we send the beams down a path about 12 m long and aligned through two irises. This setup should provide an angular tolerance of around 0.08 mrad and is drawn in Figure A.1.

Thus, while the original placement of the beams must first be achieved by ensuring that they pass through the centers of the vacuum chamber windows. Our alignment setup allows the three beams to be well-overlapped with each other.

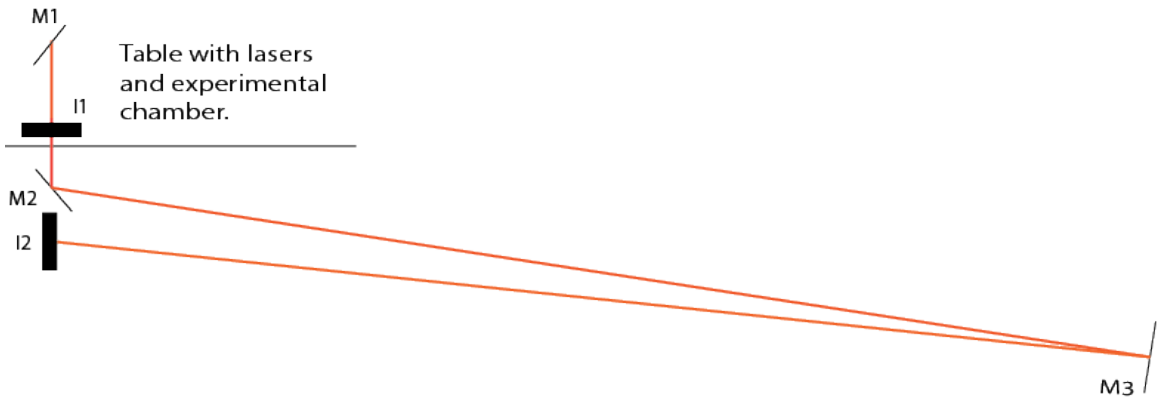

Figure A.1: A diagram of the alignment setup we use to spatially overlap our beams to an angular tolerance of 0.08 mrad. The beams drawn here have been redirected from going into the vacuum chamber and sent down this long alignment arm. Note that this figure is not drawn to scale. The direct distance from I1 to I2 is 0.3 m and the distance from M2/I2 to M3 is 5.4 m.

A.2 Retroreflection Alignment

To cancel the first-order Doppler shift on the vibrational transition lines, we retroreflect the 767-nm beam using a spherical mirror on the far end of the cavity. Again, because the spatial overlap of the forward- and back-propagating beam waists is essential, this mirror must be carefully aligned.

The mirror is mounted on a three-knob mirror mount attached to the vacuum chamber via four rods. These three knobs allow us to slightly adjust the translation as well as the angle of the mirror.

The mirror is transparent to the two UV beams (when we use the 355-nm dissociation beam). So, we do not need to worry about the pulse being reflected back into the laser cavity. When using the 266-nm dissociation beam, our mirror is no longer transparent and so we use a dichroic before the retroreflecting mirror to dump the UV beams. However, with the beams being perfectly reflected back, we must ensure that they do not reach the laser cavities, as that would damage our lasers. So, we place an optical isolator close to the SIRAH dye laser.

We ensure that the retroreflection is well-aligned by viewing the reflected IR beam

on a mostly closed iris. Viewing this beam allows us to center the reflected beam on the iris. Additionally, the returning beam, which is rejected by the optical isolator, is split into two outgoing beams by the polarizer. Final alignment can be carried out by ensuring that these have a comparable shape to the original beam.

A.3 Focusing the light - Achromatic Lenses

We use a large range of wavelengths in our experiment, which can make finding effective lens material difficult. Typical lens material (we use UV fused silica) focus the REMPI (301 nm) beam and the vibrational (767 nm) beam at different locations, specifically 17 Rayleigh Ranges in the 767 nm beam (or 6.9 mm away) from each other. Thus, since the transition rates for both the REMPI and vibrational transitions rely on the intensity, such a lack in focus would deeply cut into our signal.

As the lead time for commercial achromatic lenses was long, Professor Hanneke designed one, which has a 3.77 mm focal length shift between 266 nm - 800 nm.

The high intensity laser beams in our experiment lead to this achromatic lens being burnt. Essentially, a small amount of light was reflected by the vacuum chamber window, which was close to halfway between the lens and the focus. Thus, this reflected light was nearly focused on the lens and so machined a hole in the center.

Appendix B

Timing

The timing of each step in the experiment is critical. The experiment is controlled by one central computer, which has a clock that runs at 20 MHz. While the clock itself has low jitter, a frequency of 20 MHz means that each clock cycle is 50 ns. The timing of our lasers needs to be more precisely controlled than this. The timing of the photoionizing laser is adjusted more precisely by adding coaxial cable length to the cable that carries the trigger.

In Figure B.1, we see the trigger sequence. The Quantel Nd:YAG flashlamps fire twice during our experiment cycle, but we only turn on the Q-switch for the second shot, because we wish to run at a rate of 10 Hz and the flashlamps fire at 20 Hz. Now that we trigger the gas valve slightly earlier because it takes time both for the gas valve to fully open and for the gas to travel to the experimental region. The Innolas flashlamps and Pockels cell triggers decide both when the Innolas Nd:YAG fires *and* the energy of the beam. Particularly, the energy depends on the Pockels cell delay. I do wish to additionally clarify in Figure B.1 that the electrodes takes a certain amount of time (around 100 ns) to ramp up after the trigger. Thus, while the electrodes appear to turn on at the same time the Quantel Nd:YAG fires, in actuality they ramp up afterwards.

Additionally, both the infrared pulse that excites the vibrational transition and the UV dissociating laser originate from the same ND:YAG laser and, thus, cannot have their timing controlled electronically. So, we add optical path length to the UV pulse in order to ensure that it arrives after the IR pulse.

The pulses each arrive about 15 ns after the other. We can check this timing by looking at the times that each beam arrives at our photodetector. Our relative timing can be seen in Figure B.2.

One of the reasons for making sure that the pulses are close in time is that the beam waist is relatively small (compared to the experimental region as a whole). We must ensure that the molecules remain in the beam waist long enough for the entire experimental sequence to occur. In particular, if the electrodes are left on at their full voltages, a molecule will be accelerated through the distance of the beam waist in 61 ns. Thus, in addition to making sure that the lasers are relatively close in time, as above, we pulse the electrodes as well. This idea has already been brought up in my thesis earlier, but the following section goes into greater detail on the process.

B.1 Electrode Pulsing

In addition to tweaking the timing of the pulses, we also pulse the electrode voltages using a high-voltage logic circuit, developed by Addison Hartman. These voltages accelerate the ions out of the experimental region and towards a detector (and will be discussed more in the following section). We nominally turn the voltages on after the transitions have been driven. Currently, we are running the experiment so that the voltages turn on 1 μs after the trigger goes to the photoionization laser Q-switch. We cannot say exactly when the electrodes reach their full voltage relative to the transitions being driven. A similar board was measured in a test environment with about 100 ns rise time. We tried multiple different delays for the voltages. At 1 μs,

the number of ions was slightly decreased from a 0 μs delay and the time of arrival was shifted. Out at 2 μs delay, the signal was significantly lower. We believe that this is due to the molecules leaving the experimental region due to 1) the velocity of the gas beam or 2) the Coulomb repulsion between the ions after photoionization. Thus, we cannot quantify the exact delay between the ions being created and the high voltages ramping up. However, we cannot be perfectly sure when the ions are being accelerated out of the experimental region.

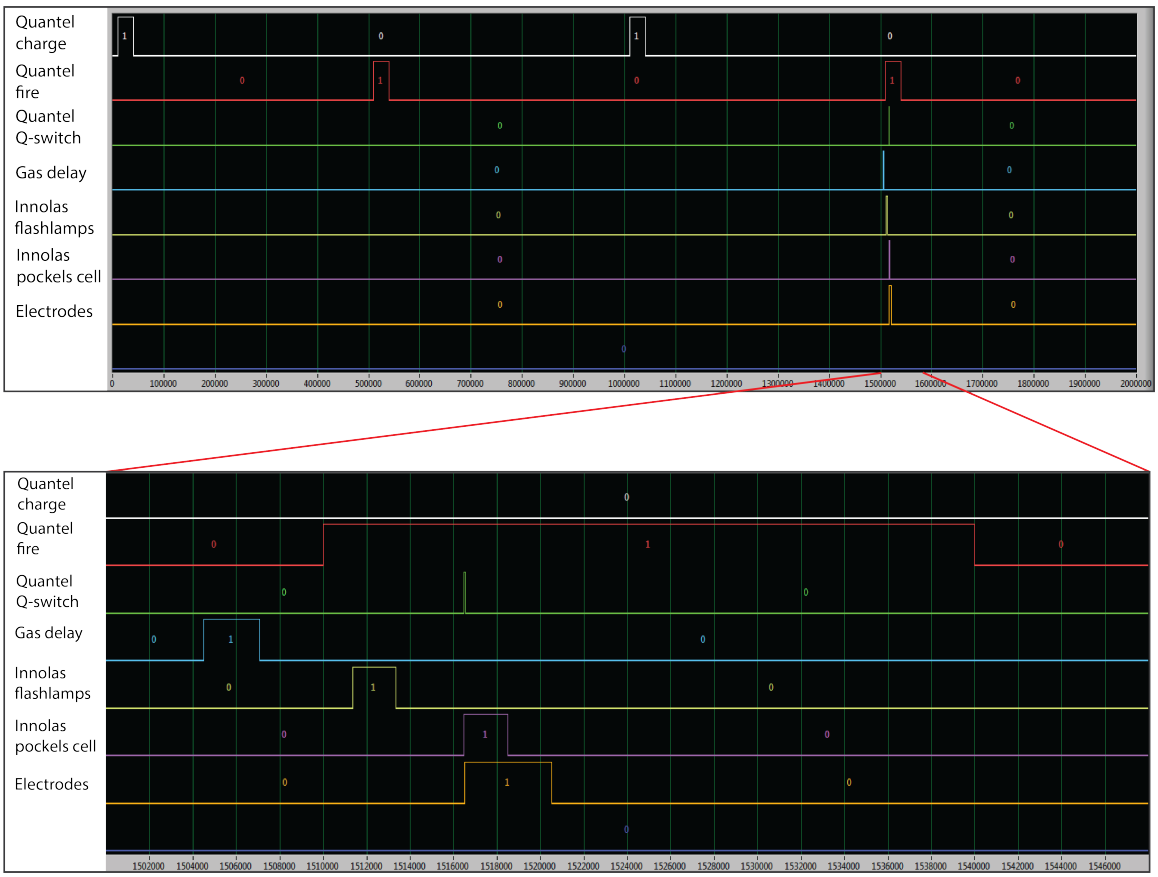

Figure B.1: Our triggering sequence above shows the full 0.1 s of each step a zoomed in view of the above. Note that this sequence is plotted in terms of clock-cycles from 0 to 2,000,000 clock cycles (so 0 to 0.1 s). The Quantel Nd:Yag flashlamps fire at a rate of 20 Hz, but we run the experiment at a rate of 10 Hz due to the Innolas flashlamps. Also, "Quantel fire" refers to firing the flashlamps, and the laser does not actually lase until the Q-switch is triggered. Keep in mind that the triggering sequence cannot show how long it takes some of the events to occur, particularly for the Gas Delay trigger and the Electrodes trigger.

(a) Relative timing of the REMPI and IR beams

(b) Relative timing of IR and dissociation (UV) beams

Figure B.2: Both figures show our full oscilloscope trace. The yellow line is the amplified signal from the MCP, and the blue line is the signal from our photodetector. For each blue peak, we blocked the other two lasers and then used the cursor to estimate the time at which the peak reached half-height. Doing the same with the next laser and leaving persist on (as seen above) gives a decent estimate of the relative timing.

Appendix C

Scan with 355 nm dissociation

This appendix is written to supplement the data shown in Figure 4.8a. The mass ranges are given quite conservatively in the captions, but should offer a rough picture of what we would expect to find, given these different time bins.

These other bins primarily serve to confirm that we have not seen any signal yet. The larger time bins are similarly noisy, just higher amplitude, than the smallest O^+ bin. Furthermore, the control bins (bin 5 and bin 6) have slightly lower peaks, but not extremely so.

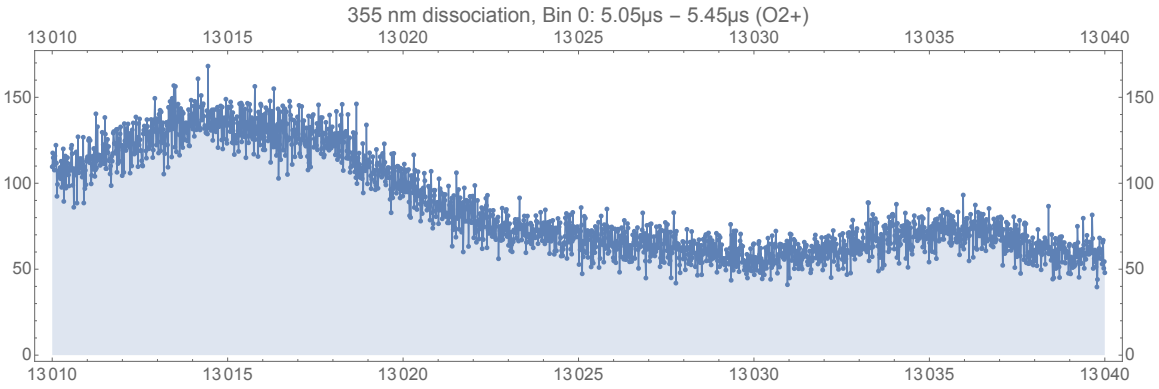

Figure C.1: The first bin (bin 0) is centered at 5.25 μs and catches our molecular ions. So, the time range is t = 5.05 μs - 5.45 μs and the mass is m = 32 amu.

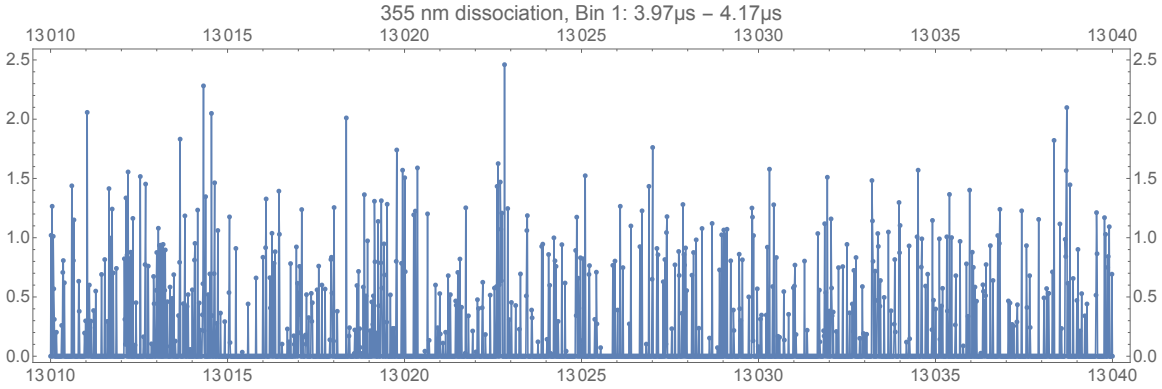

This is our narrowest time bin for oxygen atomic ions. The time range is t = 3.97 μs - 4.17 μs, which corresponds to a mass of m = 16 amu.

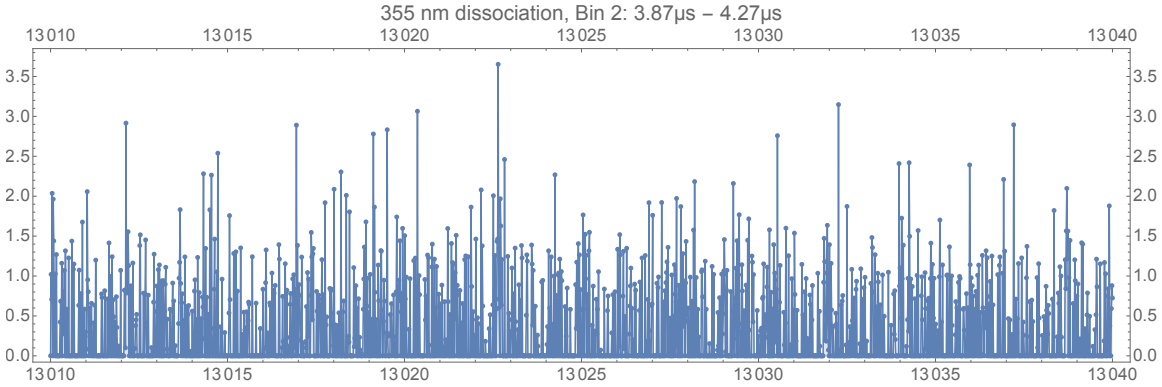

This is a slightly wider time bin, still centered on where we predict the oxygen atomic ions to arrive. The time range is t = 3.87 μs - 4.27 μs, which corresponds a range of m = 15 - 17 amu.

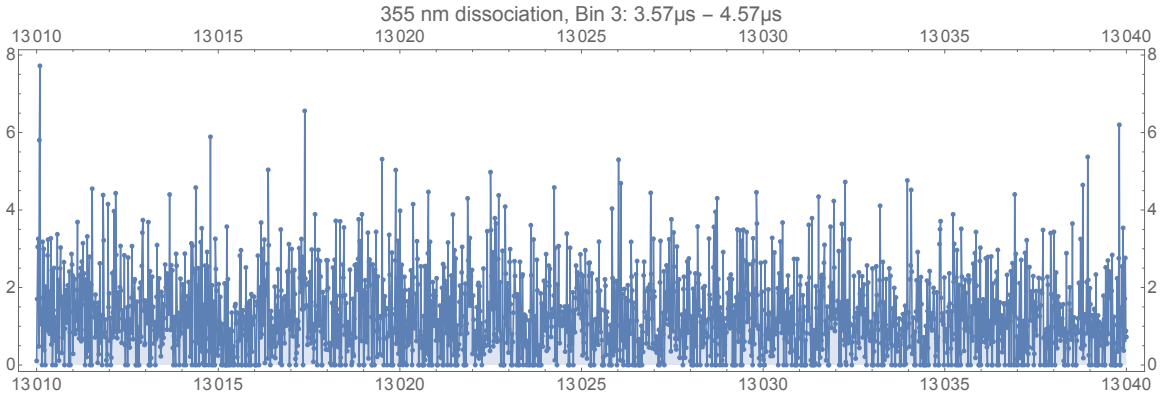

This is our largest time bin, centered on oxygen atomic ions. The time range is 3.57 μs - 4.57 μs, which corresponds to a mass range of m = 12-22 amu. We would expect to see fair amounts of noise here.

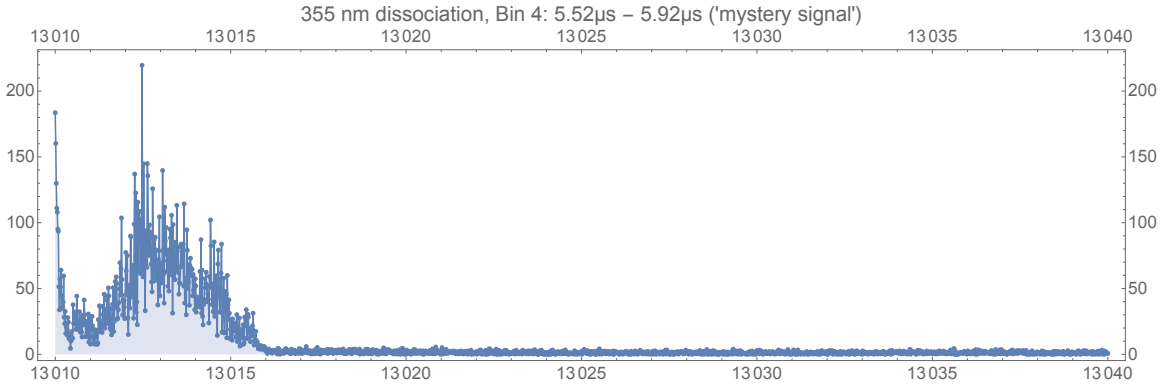

This is our 'mystery signal' bin, and you can see some strange signal which seems to conflict with what we had seen previously in Figure 4.11. The time range is 5.52 μs - 5.92 μs, which corresponds to a mass range m = 37-44 amu.

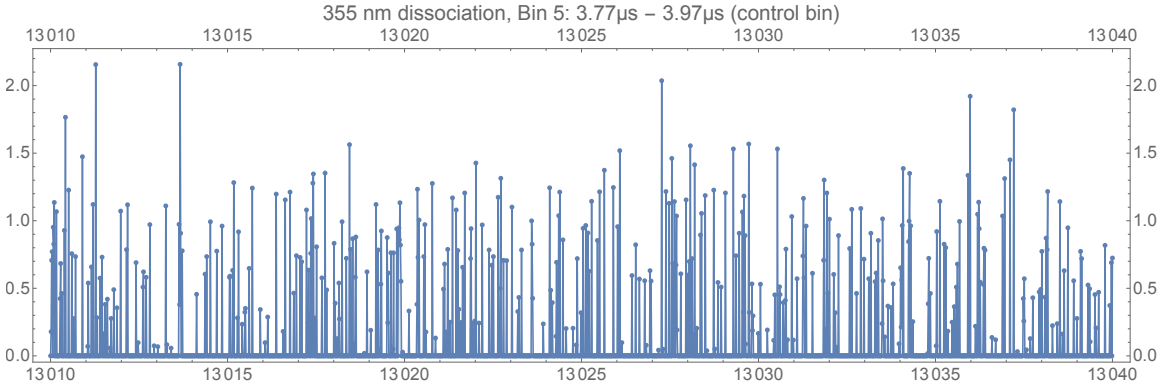

This is our first control bin, positioned before we expect to see signals for atomic oxygen. The time range is 3.77 μs - 3.97 μs, which corresponds to a mass of about m = 14 amu.

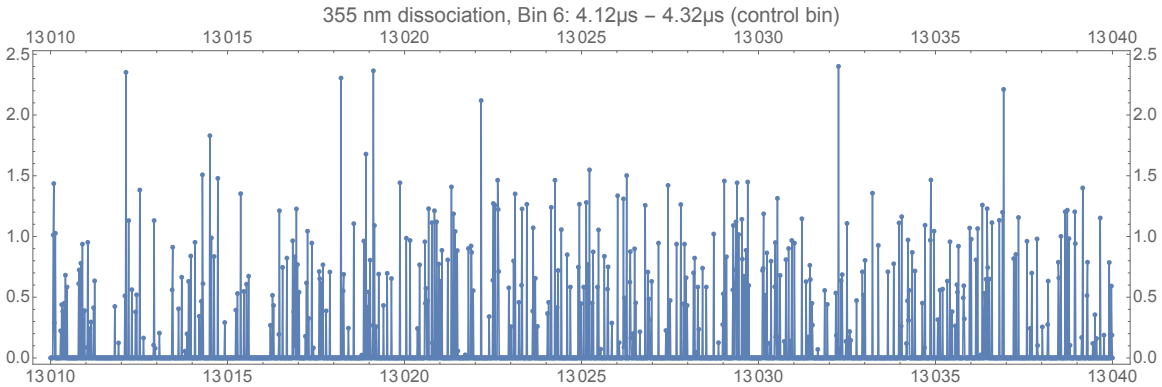

This is our second control bin, positioned just after we expect to see signals for atomic oxygen. The time range is 4.12 μs - 4.32 μs, which corresponds to a mass range of about m = 17-19 amu.

Appendix D

Scan with 266 nm dissociation

Similarly to Appendix C, this appendix provides plots to give some context to the example data shown in Figure 4.8b.

Here, you can see the molecular-ion production as well as the ions that fall into each time bin. Overall, there are far more ions here than for the 355 nm dissociation.

There are still no clear signals anywhere. Strangely, the 'signal' (or lack thereof) seen for bin 4 in the figures below differs from all examples of the 'mystery signal' that we had seen before in Figures 4.11 and 4.11.

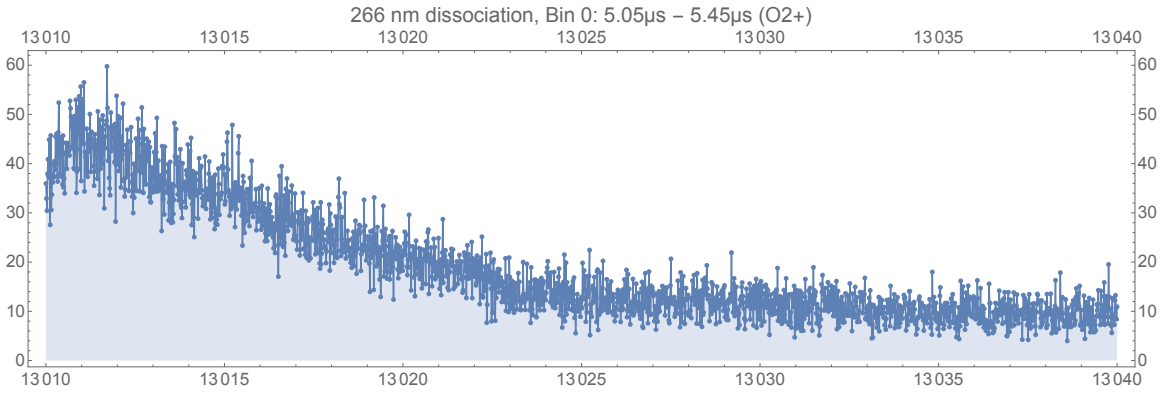

Figure D.1: The first bin (bin 0) is centered at 5.25 μs and catches our molecular ions. So, the time range is t = 5.05 μs - 5.45 μs and the mass is m = 32 amu.

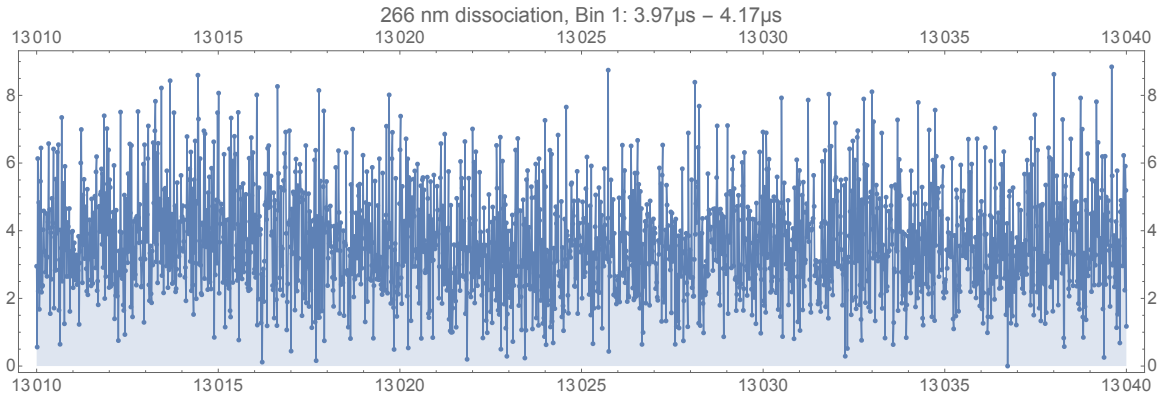

This is our narrowest time bin for oxygen atomic ions. The time range is t = 3.97 μs - 4.17 μs, which corresponds to a mass of m = 16 amu.

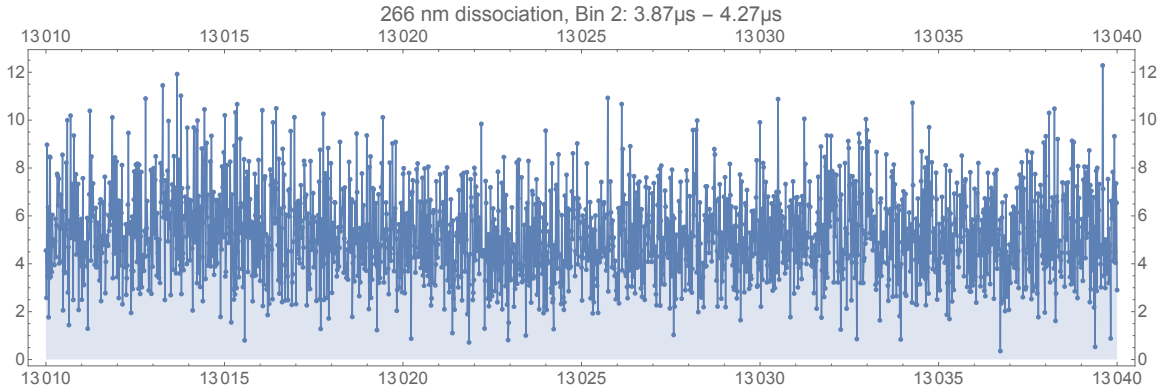

This is a slightly wider time bin, still centered on where we predict the oxygen atomic ions to arrive. The time range is t = 3.87 μs - 4.27 μs which corresponds a range of m = 15 - 17 amu.

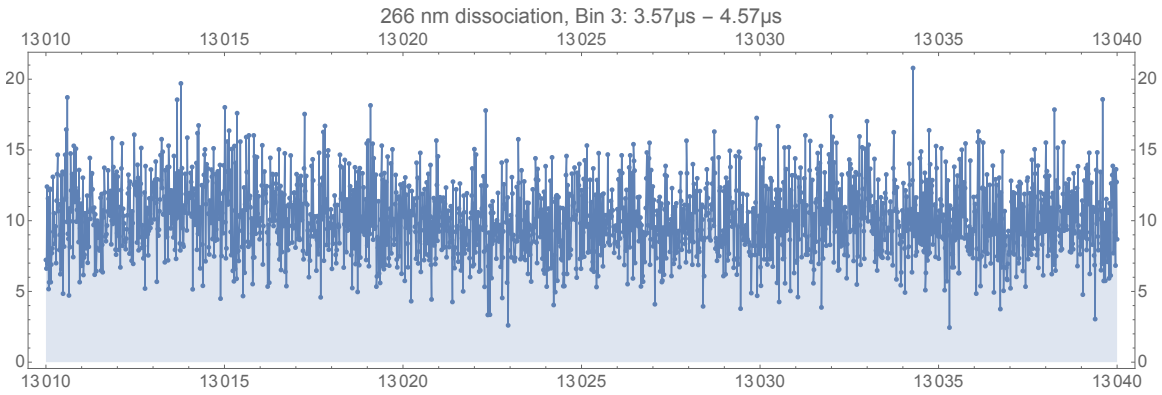

This is our largest time bin, centered on oxygen atomic ions. The time range is 3.57 μs - 4.57 μs, which corresponds to a mass range of m = 12-22 amu.

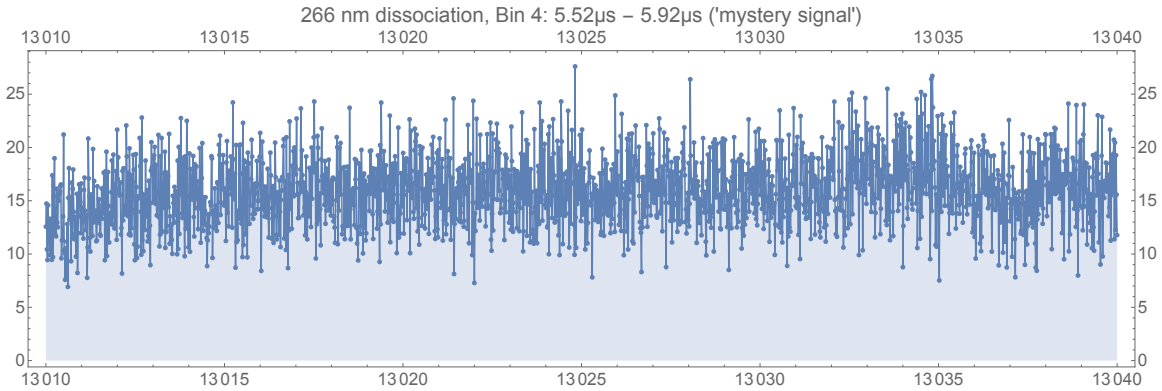

This is our 'mystery signal' bin. Here, no obvious signal is present, and we seem to see only noise unlike the 'mystery signal' in Appendix C and in Figure 4.11. The time range is 5.52 μs - 5.92 μs, which corresponds to a mass range m = 37-44 amu.

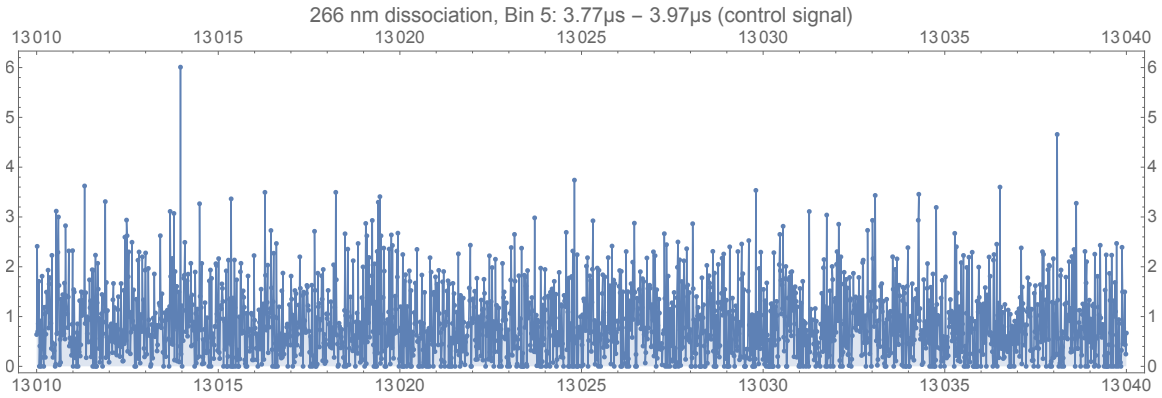

This is our first control bin, positioned before we expect to see signals for atomic oxygen. The time range is 3.77 μs - 3.97 μs, which corresponds to a mass of about m = 14 amu.

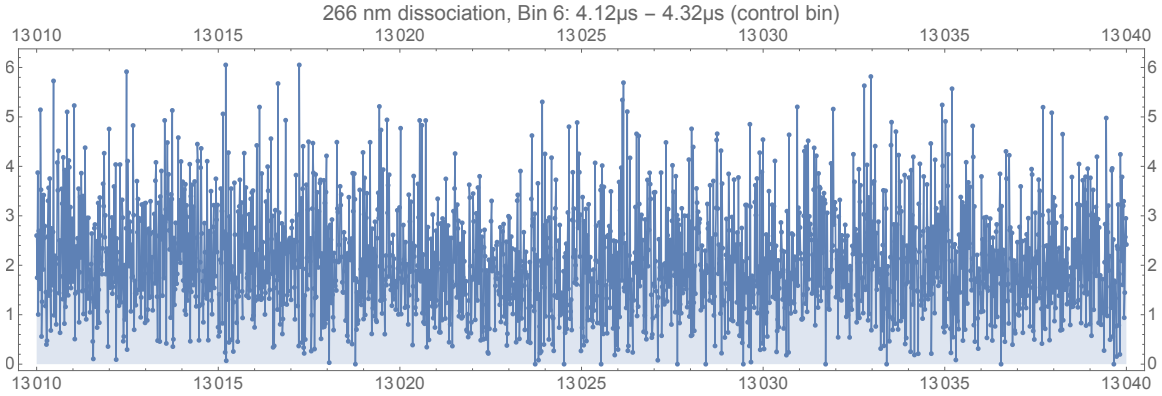

This is our second control bin, positioned just after we expect to see signals for atomic oxygen. The time range is 4.12 μs - 4.32 μs, which corresponds to a mass range of about m = 17-19 amu.

Bibliography

[1] Kenath Arun, S.B. Gudennavar, and C. Sivaram. "Dark matter, dark energy, and alternate models: A review". In: *Advances in Space Research* 60.1 (2017), pp. 166–186. ISSN: 0273-1177. DOI: https://doi.org/10.1016/j.asr.2017.03.043. URL: https://www.sciencedirect.com/science/article/pii/S027311771730248X.

[2] Asimina Arvanitaki, Junwu Huang, and Ken Van Tilburg. "Searching for dilaton dark matter with atomic clocks". In: *Physical Review D* 91 (1 Jan. 2015), p. 015015. DOI: 10.1103/PhysRevD.91.015015. URL: https://link.aps.org/doi/10.1103/PhysRevD.91.015015.

[3] F. Brandi and F. Giammanco. "Temporal and spatial characterization of a pulsed gas jet by a compact high-speed high-sensitivity second-harmonic interferometer". In: *Optics Express* 19.25 (Dec. 2011), p. 25479. DOI: 10.1364/oe.19.025479.

[4] John M Brown and Alan Carrington. *Rotational spectroscopy of diatomic molecules*. Cambridge Cambridge Univ. Press, 2003. ISBN: 9780521530781.

[5] Ryan Carollo, Alexander Frenett, and David Hanneke. "Two-Photon Vibrational Transitions in $^{16}O_2^+$ as Probes of Variation of the Proton-to-Electron Mass Ratio". In: *Atoms* 7 (2018), p. 1. DOI: 10.3390/atoms7010001.

[6] Riccardo Catena and Piero Ullio. "A novel determination of the local dark matter density". In: *J. Cosmology Astroparticle Phys.* 2010 (2010), p. 004. DOI: 10.1088/1475-7516/2010/08/004.

[7] Eric Cornell. "The Three-Legged Stool". In: DAMOP. Milwaukee, WI, 2019.

[8] D. G. Fedorov et al. "Theoretical study of spin-orbit coupling constants for O_2^+ ($A^2\Pi_{3/2,1/2u}$, $v^+ = 0$–17 and $a^4\Pi_{5/2,3/2,1/2,1/2u}, v+ = 0$–25)". In: *The Journal of Chemical Physics* 115.16 (Oct. 2001), pp. 7393–7400. DOI: 10.1063/1.1402170.

[9] V. V. Flambaum and A. F. Tedesco. "Dependence of nuclear magnetic moments on quark masses and limits on temporal variation of fundamental constants from atomic clock experiments". In: *Physical Review C* 73 (2006), p. 055501. DOI: 10.1103/PhysRevC.73.055501.

[10] Alex Frenett. "State-selective Production of Oxygen Molecular Ions for New Physics Searches". Undergraduate thesis. Amherst College, 2018.

[11] Mary K. Gaillard, Paul D. Grannis, and Frank J. Sciulli. "The standard model of particle physics". In: *Rev. Mod. Phys.* 71 (2 Mar. 1999), S96–S111. DOI: 10.1103/RevModPhys.71.S96. URL: https://link.aps.org/doi/10.1103/RevModPhys.71.S96.

[12] Katherine Garrett and Gintaras Duda. "Dark Matter: A Primer". In: *Advances in Astronomy* 2011 (2011), p. 968283. DOI: 10.1155/2011/968283.

[13] Matthias Germann, Xin Tong, and Stefan Willitsch. "Observation of electric-dipole-forbidden infrared transitions in cold molecular ions". In: *Nature Physics* 10 (2014), pp. 820–824. DOI: 10.1038/NPHYS3085.

[14] Matthias Germann and Stefan Willitsch. "Fine- and hyperfine-structure effects in molecular photoionization. I. General theory and direct photoionization". In: *The Journal of Chemical Physics* 145 (2016), p. 044314. DOI: 10.1063/1.4955301.

[15] D. Hanneke, R. A. Carollo, and D. A. Lane. "High sensitivity to variation in the proton-to-electron mass ratio in O_2^+". In: *Physical Review A* 94 (2016), 050101(R). DOI: 10.1103/PhysRevA.94.050101.

[16] David Hanneke. *Private communication*.

[17] David Hanneke, Boran Kuzhan, and Annika Lunstad. "Optical clocks based on molecular vibrations as probes of variation of the proton-to-electron mass ratio". In: *Quantum Science and Technology* 6 (2021), p. 014005. DOI: 10.1088/2058-9565/abc863. arXiv: 2007.15750.

[18] Aurélien Hees et al. "Violation of the equivalence principle from light scalar dark matter". In: *Physical Review D* 98 (6 Sept. 2018), p. 064051. DOI: 10.1103/PhysRevD.98.064051. URL: https://link.aps.org/doi/10.1103/PhysRevD.98.064051.

[19] Gerhard Herzberg. *Molecular Spectra and Molecular Structure, Vol. I: Spectra of Diatomic Molecules*. D. Van Nostrand Co., 1950. ISBN: 0894642685.

[20] Michael Hippler. "Interference in two-photon rotational line strengths of diatomic molecules". In: *Molecular Physics* 97.1-2 (July 1999), pp. 105–116. DOI: 10.1080/00268979909482813.

[21] Paulus Jauernik. *Precision scan and Cobra Stretch Datasheet*. 2021.

[22] J. Kobayashi, A. Ogino, and S. Inouye. "Measurement of the variation of electron-to-proton mass ratio using ultracold molecules produced from laser-cooled atoms". In: *Nature Comm.* 10 (2019), p. 3771. DOI: 10.1038/s41467-019-11761-1.

[23] Mark G. Kokish et al. "Prospects for Polar-Molecular-Ion Optical Probe of Varying Proton-Electron Mass Ratio". In: *Physical Review A* 98 (2018), p. 052513. DOI: 10.1103/PhysRevA.98.052513.

[24] S. S. Kondov et al. "Molecular lattice clock with long vibrational coherence". In: *Nature Physics* 15 (2019), pp. 1118–1122. DOI: 10.1038/s41567-019-0632-3.

[25] Ivan Kozyryev, Zack Lasner, and John M. Doyle. "Enhanced Sensitivity to Ultralight Bosonic Dark Matter in the Spectra of the Linear Radical SrOH". In: *Physical Review A* 103.4 (Apr. 2021), p. 043313. DOI: 10.1103/PhysRevA.103.043313.

[26] Boran Kuzhan. "A Molecular Beam Apparatus to Search for Time-Variation of Fundamental Constants". Undergraduate thesis. Amherst College, 2021.

[27] David A. Lane. "Developing a Quantum Toolbox: Experiments with a Single-Atom Harmonic Oscillator and Prospects for Probing Molecular Ions". Undergraduate thesis. Amherst College, 2017.

[28] Robert Le Roy and Geoffrey Kraemer. *BCONT 2.2: A Computer Program for Calculating Bound → Continuum Transition Intensities for Diatomic Molecules Chemical Physics Research Report*. 2004. URL: http://www.ace.uwaterloo.ca/leroy/BCONT/BCONTDraftMan.pdf.

[29] Hui Liu et al. "Accurate theoretical spectroscopic investigations of the 20 Λ-S and 58 Ω states of O_2^+cation including the spin–orbit coupling effect". In: *Molecular Physics* 113.2 (Aug. 2014), pp. 120–136. DOI: 10.1080/00268976.2014.948516.

[30] Jiangli Liu, Xun Chen, and Xiangdong Ji. "Current status of direct dark matter detection experiments". In: *Nature Physics* 13 (2017), pp. 212–216. DOI: 10.1038/nphys4039.

[31] C. Maïnos. "Multiphoton rotational line strength in diatomic molecules and for states with Hund's case-(a) or case-(b) coupling". In: *Physical Review A* 33.6 (June 1986), pp. 3983–3992. DOI: 10.1103/physreva.33.3983.

[32] K.A. Olive. "Review of Particle Physics". In: *Chinese Physics C* 40.10 (Oct. 2016), p. 100001. DOI: 10.1088/1674-1137/40/10/100001.

[33] Julia Pfatteicher. "Developing Rapid Quenching Electronics for Coupling an Ion Trap to a Mass Spectrometer". Undergraduate thesis. Amherst College, 2019.

[34] Shenglan Qiao. "Constructing a Linear Paul Trap System for Measuring Time-variation of the Electron-Proton Mass Ratio". Undergraduate thesis. Amherst College, 2013.

[35] M. S. Safronova et al. "Search for new physics with atoms and molecules". In: *Review of Modern Physics* 90 (2018), p. 025008. DOI: 10.1103/RevModPhys.90.025008.

[36] S. Schiller, D. Bakalov, and V. I. Korobov. "Simplest Molecules as Candidates for Precise Optical Clocks". In: *Physical Review Letters* 113 (2014), p. 023004. DOI: 10.1103/PhysRevLett.113.023004.

[37] S. Schiller and V. Korobov. "Tests of time independence of the electron and nuclear masses with ultracold molecules". In: *Physical Review A* 71 (2005), p. 032505. DOI: 10.1103/PhysRevA.71.032505.

[38] S. Schlamminger et al. "Test of the Equivalence Principle Using a Rotating Torsion Balance". In: *Phys. Rev. Lett.* 100 (4 Jan. 2008), p. 041101. DOI: 10.1103/PhysRevLett.100.041101. URL: https://link.aps.org/doi/10.1103/PhysRevLett.100.041101.

[39] P. O. Schmidt et al. "Spectroscopy Using Quantum Logic". In: *Science* 309 (2005), pp. 749–752. DOI: 10.1126/science.1114375.

[40] Christopher M. Seck et al. "Rotational state analysis of AlH^+ by two-photon dissociation". In: *Journal of Molecular Spectroscopy* 300 (2014), pp. 108–111. ISSN: 0022-2852. DOI: 10.1016/j.jms.2014.03.023.

[41] A. Sharma et al. "Counting the electrons in a multiphoton ionization by elastic scattering of microwaves". In: *Scientific Reports* 8.1 (Feb. 2018). DOI: 10.1038/s41598-018-21234-y.

[42] Anthony E Siegman. *Lasers*. Univ. Science Books, 1986.

[43] Mudit Sinhal et al. "Quantum-nondemolition state detection and spectrocsopy of single trapped molecules". In: *Science* 367 (2020), pp. 1213–1218. DOI: 10.1126/science.aaz9837.

[44] Y. Song et al. "Rotationally resolved pulsed field ionization photoelectron bands of $O_2^+(X\,^2\Pi_{1/2,3/2g}, v^+ = 0 - 38)$ in the energy range of $12.05 - 18.15$ eV". In: *The Journal of Chemical Physics* 111 (1999), pp. 1905–1916. DOI: 10.1063/1.479459.

[45] Peter F. Staanum et al. "Rotational laser cooling of vibrationally and translationally cold molecular ions". In: *Nature Physics* 6.4 (Apr. 2010), pp. 271–274. DOI: 10.1038/nphys1604. URL: https://www.nature.com/articles/nphys1604.

[46] Y. V. Stadnik and V. V. Flambaum. "Can Dark Matter Induce Cosmological Evolution of the Fundamental Constants of Nature?" In: *Physical Review Letters* 115 (2015), p. 201301. DOI: 10.1103/PhysRevLett.115.201301.

[47] Y. V. Stadnik and V. V. Flambaum. "Improved limits on interactions of low-mass spin-0 dark matter from atomic clock spectroscopy". In: *Physical Review A* 94 (2016), p. 022111. DOI: 10.1103/PhysRevA.94.022111.

[48] University of Toronto. *Laser Safety Training Manual*. URL: https://ehs.utoronto.ca/laser-safety-training-manual/.

[49] C. M. Western. *PGOPHER*. Version 10.1. 2018. DOI: doi:10.5523/bris.3mqfb4glgkr8a2rev7f73t300c..

[50] W. C. Wiley and I. H. McLaren. "Time-of-Flight Mass Spectrometer with Improved Resolution". In: *Review of Scientific Instruments* 26 (1955), pp. 1150–1157. DOI: 10.1063/1.1715212.

[51] Fabian Wolf et al. “Prospect for precision quantum logic spectroscopy of vibrational overtone transitions in molecular oxygen ions”. In: (2020). arXiv:2002.05584. arXiv: 2002.05584 [physics.atom-ph].

[52] Jinchun Xie and Richard N. Zare. “Selection rules for the photoionization of diatomic molecules”. In: *The Journal of Chemical Physics* 93.5 (Sept. 1990), pp. 3033–3038. DOI: 10.1063/1.458837.

[53] Aaron W. Young et al. “Half-minute-scale atomic coherence and high relative stability in a tweezer clock”. In: *Nature* 588.7838 (Dec. 2020), pp. 408–413. DOI: 10.1038/s41586-020-3009-y.

[54] T. Zelevinsky, S. Kotochigova, and Jun Ye. “Precision Test of Mass-Ratio Variations with Lattice-Confined Ultracold Molecules”. In: *Physical Review Letters* 100 (2008), p. 043201. DOI: 10.1103/PhysRevLett.100.043201.